

Exploring Effects in Tippers at Island Geomagnetic Observatories Due to Realistic Depth- and Time-varying Oceanic Electrical Conductivity

Rafael Rigaud (✉ rafael.rigaud@hotmail.com)

Observatorio Nacional <https://orcid.org/0000-0002-2299-6430>

Mikhail Kruglyakov

Institute of Physics of the Earth, Troitsk, Russia

Alexey Kuvshinov

ETH-Zürich

Katia J Pinheiro

Observatório Nacional

Johannes Petereit

GFZ Potsdam

Juergen Matzka

GFZ Potsdam

Elena Marshalko

ETH-Zürich

Full paper

Keywords: Ocean induction effect, tippers, 3-D electromagnetic modeling, island geomagnetic observatories, oceanic 24 electrical conductivity

Posted Date: October 29th, 2020

DOI: <https://doi.org/10.21203/rs.3.rs-98556/v1>

License: © ⓘ This work is licensed under a Creative Commons Attribution 4.0 International License.

[Read Full License](#)

Version of Record: A version of this preprint was published on January 4th, 2021. See the published version at <https://doi.org/10.1186/s40623-020-01339-3>.

1 **Exploring Effects in Tippers at Island Geomagnetic Observatories**
2 **due to Realistic Depth- and Time-Varying Oceanic Electrical**
3 **Conductivity**

4 Rafael Rigaud^{1,2*}, Mikhail Kruglyakov^{2,3}, Alexey Kuvshinov², Katia J. Pinheiro¹, Johannes
Petereit⁴, Juergen Matzka⁴ and Elena Marshalko^{2,5,6}

*Correspondence: rafael.rigaud@erdw.ethz.ch

6 **Abstract**

7 Vertical magnetic transfer functions (tippers) estimated at island observatories can constrain the
8 one-dimensional (1-D) conductivity distribution of the oceanic lithosphere and upper mantle. This is
9 feasible due to the bathymetry-dependent ocean induction effect (OIE), which originates from lateral
10 conductivity contrasts between ocean and land and leads to non-zero tippers even for 1-D conductivity
11 distributions below the ocean. Proper analysis of island tippers requires accurate three-dimensional
12 (3-D) modeling of the OIE, for which so far was performed assuming constant sea water electric
13 conductivity with depth. In this study we explore – using rigorous 3-D electromagnetic modeling – to
14 what extent realistic, depth-dependent, oceanic conductivity affects island tippers. The modeling is
15 performed for eleven island observatories around the world in the period range 10^{-1} to 10^4 sec. We also
16 investigate the effect of seasonal variations of the oceanic conductivity and to which extent this could
17 explain the observed systematic seasonal variation of tippers. Our model studies suggest that for most
18 of the considered island observatories the effect from depth-varying oceanic conductivity is tangible and
19 exceeds the error floor of 0.025, which usually is assigned to tippers during their inversion. The effect
20 varies significantly with location, depending on regional bathymetry. Contrarily, the effects from
21 seasonally varying oceanic conductivity were found to be too small to be worth consideration.

22 **Keywords**

23 Ocean induction effect, tippers, 3-D electromagnetic modeling, island geomagnetic observatories, oceanic
24 electrical conductivity

25 **Introduction**

26 One of the geophysical methods to probe the physical parameters of the Earth's mantle is Geomagnetic
27 Depth Sounding (GDS; Banks, 1969; Weidelt, 1972). GDS exploits magnetic field variations of magneto-
28 spheric and/or ionospheric origin and allows to constrain electrical conductivity at depth. The main data
29 source for GDS are magnetic field measurements performed at the global net of geomagnetic observatories.
30 Long-period (> 3 hours) variations are routinely used in GDS to constrain electrical conductivity of the
31 Earth's mantle (approximately from 400 km down to 1500 km) either in terms of local one-dimensional

32 (1-D; Olsen, 1998; Utada et al, 2003; Munch et al, 2018; Chen et al, 2020; Zhang et al, 2020, among
 33 others) or three-dimensional (3-D; Kelbert et al, 2009; Semenov and Kuvshinov, 2012; Koyama et al,
 34 2014; Sun et al, 2015; Li et al, 2020, among others) conductivity distributions.
 35 Recent studies (Samrock and Kuvshinov, 2013; Morschhauser et al, 2019) have also shown that vertical
 36 transfer functions (tippers) estimated from short-period (< 3 hours) variations at island observatories
 37 can be used to constrain conductivity distribution beneath oceans where our knowledge is still very
 38 limited. This becomes feasible due to the ocean induction effect (OIE; cf. Parkinson and Jones, 1979),
 39 which originates from lateral conductivity contrasts between ocean and land. The OIE leads to non-
 40 zero tippers even for 1-D conductivity distribution beneath the ocean (cf. Samrock and Kuvshinov,
 41 2013), therefore the inversion of island tippers can provide information on the electrical properties of
 42 the crust and upper mantle in remote oceanic regions. However, the interpretation of island tippers
 43 requires accurate 3-D electromagnetic (EM) modeling of the OIE that takes into account the bathymetry
 44 around the observatory. Hitherto, during such modeling the researchers assumed constant oceanic electric
 45 conductivity with depth (cf. Samrock and Kuvshinov, 2013; Morschhauser et al, 2019). In many regions
 46 of the world, however, oceanic conductivity varies significantly within the uppermost few hundred meters
 47 of the water column (cf. Tyler et al, 2017). In this study we explore the extent to which realistic
 48 depth-varying oceanic conductivity affects island tippers. Our analysis is performed for eleven island
 49 observatories located in the Pacific, Atlantic and Indian Oceans (cf. Figure 1). In addition, we investigate
 50 the effect of seasonal variations of oceanic conductivity and to which extent this could explain the
 51 systematic seasonal variations in tippers investigated by Araya Vargas and Ritter (2016) and attributed
 52 to the variability of external magnetic source fields.

53 **Methods**

54 **Tippers**

55 In non-polar regions, the source of the magnetic field variations with periods shorter than 3 hours is
 56 well approximated by a vertically incident plane wave. The plane wave assumption allows one to
 57 relate the vertical component B_z with the horizontal component $\mathbf{B}_H = (B_x \ B_y)$ via the so-called tipper
 58 $\mathbf{T} = (T_{zx} \ T_{zy})$ (e.g. Berdichevsky and Dmitriev, 2008)

$$B_z(\omega, \mathbf{r}) = T_{zx}(\omega, \mathbf{r})B_x(\omega, \mathbf{r}) + T_{zy}(\omega, \mathbf{r})B_y(\omega, \mathbf{r}), \quad (1)$$

59 where $\omega = 2\pi/P$ is the angular frequency of magnetic field variations with period P . The x - and
60 y -directions are defined in this paper as the directions to geographic North and East, respectively, and
61 z is directed vertically downwards. As a consequence of the plane-wave excitation, B_z (and thus \mathbf{T}) are
62 nonzero only above non-1-D conductivity structures. In fact one can interpret \mathbf{T} as a measure of the
63 tipping of the magnetic field out of the horizontal plane above two-dimensional or/and 3-D conductivity
64 structures.

65 **Global oceanic conductivity model**

66 The global oceanic electric conductivity model used here is that by Petereit et al (2019), which is based
67 on the Coriolis Oceanographic data set for Re-Analysis (CORA5.0, Cabanes et al, 2013) provided by
68 the Copernicus Marine Environment Monitoring Service. The model consists of monthly 3-D oceanic
69 electrical conductivity distributions for 1990 to 2016. The conductivity is computed on a lateral grid of
70 $0.5^\circ \times 0.5^\circ$ resolution and at 152 vertical levels between the sea surface and 2000 m. More details on
71 the oceanographic data set and the calculation of the global oceanic conductivity model can be found
72 in Petereit et al (2019). From 2000 m down to the ocean bottom the sea water conductivity was set to
73 3.2 S/m (cf. Tyler et al, 2017). As an example, Figure 2 presents global maps of the depth-averaged
74 oceanic conductivity for a number of depth intervals for December 2015, illustrating the fact that oceanic
75 conductivity indeed varies laterally and with depth.

76 **Constructing island 3-D conductivity models**

77 The (Cartesian) 3-D conductivity models were constructed separately for each observatory. The models
78 include a nonuniform oceanic bathymetry and a landmass with a uniform conductivity of 0.01 S/m. We
79 decided to use the same land conductivity for all observatories as a mean representative value, since we
80 did not succeed to find better data to set the land conductivity specific for each location. The landmass is
81 defined here as the upper crust from the maximum elevation down to the maximum depth of the ocean in
82 the considered region. Note that landmass conductivity of 0.01 S/m was also adopted in previous studies
83 (Morschhauser et al, 2019; Samrock and Kuvshinov, 2013) which addressed modeling of island tippers.
84 The landmass and the ocean comprise the 3-D part of the model, which is underlain by a crust and
85 mantle with the 1-D conductivity distribution (cf. Figure 3) from Grayver et al (2017). Their 1-D model
86 was obtained by joint inversion of satellite-detected tidal and magnetospheric signals and is believed to
87 represent the globally averaged 1-D conductivity profile beneath the oceans. More details on our 3-D
88 models are as follows.

89 First, we note that as far as we exploit the integral equation (IE) based solver (to be discussed in the next
90 section) to compute magnetic fields, the modeling domain is confined to the 3-D part of the model. The
91 lateral size of the 3-D modeling domain was taken as $356 \times 356 \text{ km}^2$ square with the island observatory in
92 its center. The island was placed in the center of the modeling region (laterally) to avoid potential edge
93 effects in the results. The vertical range of the domain is from the maximum topography down to the
94 maximum depth of the ocean in the region of interest. The 3-D part of the models is constructed using
95 bathymetry and topography data from the General Bathymetry Chart of the Oceans (GEBCO, 2019),
96 which is a global map compiled from a variety of sources with 15 arc sec horizontal resolution (0.46 km at
97 the equator). Bathymetry/topography is converted to Cartesian coordinates by the use of the Transverse
98 Mercator map projection and then linearly interpolated to a uniform grid with 1 km horizontal resolution.
99 Note that we performed a comprehensive model study to justify the chosen lateral size of the modeling
100 domain and cell sizes.

101 The uppermost left panel in Figures 5–15 shows the bathymetry/topography in the vicinity of the
102 corresponding island observatory. Vertically, the 3-D modeling domain was discretized in 100 m layers
103 from the maximum topography down to 1000 m depth; from 1000 m down to the maximum bathymetry in
104 the region, the domain was discretized in 500 m thick layers (see Figure 4). Oceanic conductivity within
105 each vertical layer is assumed to be constant and is set to the 3-D average value of the 2015 December
106 (or June) oceanic conductivity model for the layer’s volume. The models from 2015 year are chosen since
107 most of experimental tippers are derived from the data for this year (or adjacent years). Sedimentary
108 layers were not incorporated into the models since sediment thickness is negligible in the oceanic regions
109 considered in this study (Straume et al, 2019).

110 Outside the 3-D volume, at depths between the surface and maximum depth of the ocean, conductivity
111 is assumed to be laterally-uniform (1-D) and is set to the same oceanic conductivity profile as inside
112 the volume, underlain by the 1-D model for crust and mantle. The air conductivity is set to 10^{-8} S/m .

113 The uppermost right panel in Figures 5-14 depicts the vertical profile of oceanic conductivity (in purple),
114 calculated by horizontally averaging oceanic conductivity (Figure 2) in a $5^\circ \times 5^\circ$ region centered at the
115 considered island observatory. The panel demonstrates that the oceanic conductivity varies significantly
116 with depth down to approximately 1 km depth. Below this depth, the values are close to 3.2 S/m.

117 Furthermore, for each observatory we construct a 3-D model with a constant oceanic conductivity of 3.2
118 S/m in all vertical layers. Outside the 3-D volume, the oceanic conductivity is set to 3.2 S/m, underlain

119 by the 1-D model by Grayver et al (2017) for crust and mantle.

120 **Modeling tippers**

121 We compute magnetic fields (and then tippers) using the 3-D EM forward modeling solver PGIEM2G
122 which is based on a volume integral equation method with contracting kernel (Pankratov et al, 1995;
123 Singer, 1995), and which was presented and validated (against finite element solver by Grayver and
124 Kolev, 2015) in Kruglyakov and Kuvshinov (2018).

125 We compute tippers at 25 periods spanning the range from 10^{-1} to 10^4 sec. Note that nowadays, most
126 observatories provide magnetic field data in the form of minute means. This allows researchers to estimate
127 tippers at periods starting from approximately 300 sec. However, there is a growing investment from the
128 scientific community in providing magnetic observatory data in the form of second means, which would
129 enable estimating tippers for periods down to a few seconds. Tippers for even smaller periods can also be
130 estimated at observatory locations by performing a short-term (a few days) measurements with the use
131 of induction coils; note that the standard observatory instrument to measure magnetic field variations
132 is a fluxgate magnetometer. Bearing in mind the above considerations, we modeled tippers at periods
133 shorter than 300 sec in order to obtain an idea what is the smallest period at which ocean induction
134 effect becomes noticeable.

135 **Estimating tippers from the data**

136 We estimated tippers at nine island geomagnetic observatories from the international real-time magnetic
137 observatory network (INTERMAGNET) using definite minute-mean data that are time series of three
138 components of magnetic field. In addition, we estimated tippers at two non-INTERMAGNET island
139 observatories: St. Helena (SHE) and Santa-Maria/Azores (SMA), also using minute-mean data. Prior
140 to the tipper estimation, obvious spikes were removed from the corresponding time series. Table
141 1 summarizes information about the observatories, including the time interval used for the tipper
142 estimation. This interval varies from observatory to observatory and was selected – based on a trial
143 and error approach – to obtain smooth (with respect to period) tippers with low uncertainties.

144 For each period, data were split into overlapping tapered windows of two periods length. Data in these
145 windows were Fourier transformed, giving the spectrum of the corresponding component from 300 to
146 9600 sec. Tippers and their uncertainties were then estimated using a robust, section-averaging (Olsen,
147 1998) linear regression scheme based on the Huber norm (e.g. Aster et al, 2005; Püthe and Kuvshinov,
148 2014).

149 Results

150 Effect of depth-varying oceanic conductivity

151 Modeling results for all eleven island observatories are presented in Figures 5 – 15. In the figures, panel (a)
152 shows the bathymetry/topography map with the corresponding observatory located in the center. The
153 dashed line indicates the west-east running bathymetry/topography profile shown in panel (b). Panel (c)
154 shows the regional depth-varying oceanic conductivity down to 2000 m (purple solid line) and the constant
155 reference oceanic conductivity (3.2 S/m, dashed orange line). Panels (d) to (g) present the $\text{Re } T_{zx}$, $\text{Re } T_{zy}$,
156 $\text{Im } T_{zx}$ and $\text{Im } T_{zy}$ tipper components. Red and orange curves correspond to tippers calculated in the
157 models with depth-varying and depth-constant oceanic electrical conductivity, respectively. The blue
158 curves represent tippers and their uncertainties estimated from the data. One can see that both observed
159 and modeled tippers fulfill the property (Marcuello et al, 2005) that is often used as a plausibility check
160 for the tippers, namely, at periods where $\text{Re } T_{zx}$ or $\text{Re } T_{zy}$ reaches a maximum (or a minimum) value,
161 $\text{Im } T_{zx}$ or $\text{Im } T_{zy}$ changes the sign. Finally, panels (h) and (i) show the effect of depth-varying oceanic
162 conductivity on island tippers. This effect is assessed by the following difference

$$\Delta T_{zi} = \sqrt{(\text{Re } T_{zi}^v - \text{Re } T_{zi}^c)^2 + (\text{Im } T_{zi}^v - \text{Im } T_{zi}^c)^2} \quad (2)$$

163 where $i \in [x, y]$, and superscripts “v” and “c” correspond to the tippers calculated in the models with
164 depth-varying and depth-constant oceanic conductivity, respectively. Here, we consider the effect as non
165 negligible if it exceeds a value of 0.025, which is conventionally used as an error floor in tipper inversions
166 (e.g. Morschhauser et al, 2019; Yang et al, 2015; Tietze and Ritter, 2013; Rao et al, 2014; Bedrosian and
167 Feucht, 2014) and which is shown in the panels as horizontal dashed line.

168 Three observations can be made from panels (d)-(g) that are independent of modeling being done with
169 depth-varying or depth-constant oceanic conductivity:

170 (1) The manifestation of the OIE in the modeled tippers varies from observatory to observatory. Given
171 that depth-varying oceanic conductivity profiles (panels (c) in all figures) present similar values for all
172 observatories, except for SMA, this variability of the OIE is expected to be due to the different bathymetry
173 distributions around the islands.

174 (2) Modeled and experimental tippers agree rather well for most observatories, for the full spectrum
175 from 300 to 9600 sec, for both components and for both the real and imaginary parts. Any remaining

176 discrepancy can most probably be attributed to regional deviations of the crustal and mantle conductivity
 177 structure from the global 1-D conductivity structure used for modeling, and, partly, to limitations in
 178 bathymetry data resolution.

179 (3) The modeled OIE in tippers can be traced to periods as short as 0.2 seconds.

180 As for the effect from depth-varying oceanic conductivity it varies from observatory to observatory, from
 181 component to component, and shows different behaviour with respect to period. This variability, like the
 182 variability of OIE itself, is expected to be from the different bathymetry distributions around the islands.

183 The largest effect – reaching 0.15 – is observed at Apia observatory in $\text{Re}T_{zx}$ component.

184 **Effects of time-varying oceanic conductivity**

185 Figure 16 presents global maps of differences between December and June oceanic conductivity in the
 186 same depth intervals as in Figure 2. As expected, the difference varies laterally, it is the largest at
 187 shallower depths (reaching 20 percent of the mean value of oceanic conductivity) and decreases with
 188 depth.

189 Finally, we modeled the effect of time-varying oceanic conductivity on island tippers. The effect is assessed
 190 by analyzing the difference

$$\widehat{\Delta T_{zi}} = \sqrt{(\text{Re}T_{zi}^D - \text{Re}T_{zi}^J)^2 + (\text{Im}T_{zi}^D - \text{Im}T_{zi}^J)^2} \quad (3)$$

191 where $i \in [x, y]$ and superscripts “D” and “J” correspond to December and June results. For the
 192 observed (i.e. estimated from the data) tippers, December and June results stand for tippers, estimated
 193 from observatory data of corresponding 2015 months. As for modeled tippers, these results mean tippers
 194 calculated in 3-D models with depth-varying oceanic conductivity models for 2015 December and June
 195 months.

196 In all considered observatories, modeled ΔT_{zx} and ΔT_{zy} are very small at all periods in the 10^{-1} to 10^4
 197 sec period range. Figures 17 and 18 present observed and modeled differences as filled circles on a global
 198 map for six representative periods from 300 to 9600 sec. Observed and modeled differences are colored
 199 in Figure 17 by light and dark red, and in Figure 18 – by light and dark blue. It is clearly seen that the
 200 effect due to time-varying oceanic conductivity is negligible; indeed, the filled circles depicted the modeled
 201 difference look as “dots”. It is interesting to note that the temporal variability of the experimental tippers
 202 increases with period, and overall it is larger in T_{zy} .

203 **Conclusions**

204 In this study we performed the first ever analysis of the effects of realistic depth- and time-varying
205 oceanic electrical conductivity on island tippers. The analysis is based on 3-D EM modeling, which
206 was carried out for eleven island observatories located in the Pacific, Atlantic and Indian Oceans. The
207 conductivity models specific for each observatory were constructed using bathymetry/topography data
208 with the highest spatial resolution available (GEBCO 2019) and a 3-D, time-dependent and physics-
209 based global model of oceanic conductivity (Petereit et al, 2019). The Cartesian EM forward solver by
210 Kruglyakov and Kuvshinov (2018) was used for tippers' modeling. Modelings were performed in wide
211 period range ($10^{-1} - 10^4$ seconds) and demonstrated that ocean induction effect in tippers can be traced
212 to periods as short as 0.2 seconds.

213 The effect due to depth-varying oceanic conductivity was assessed by comparing the tippers obtained
214 from the depth-varying and depth-constant oceanic conductivity models. Our model studies show that
215 this effect is tangible in all observatories except for TDC. It exceeds the error floor of 0.025, which is
216 usually assigned to tippers during their 2-D or 3-D inversion, and reaches values of 0.1 at API, GAN
217 and HON observatories. The appearance of the effect with respect to period and its strength varies from
218 observatory to observatory. Since depth-varying conductivity profiles are rather similar for all locations,
219 such variability of the effect is most probably due to different bathymetry distributions around the islands.
220 On the contrary, the modeled effects from time-varying oceanic conductivity appeared to be too small to
221 explain the observed seasonal variations in tippers.

222 It is worth noting that introducing a more complex ocean conductivity did not lead to an improvement
223 in the agreement between modeled and experimental responses at many observatories. The most possible
224 reason for this is a deviation of local subsurface conductivity structure from the global 1-D section used
225 in the paper. Obviously in order to improve the agreement between modeling and experimental tippers
226 one needs to invert tippers for each location, and thus obtain local conductivity profile beneath each
227 island observatory. Such inversions are out of the scope of this paper but will be the subject of future
228 study. It is planned to invert island tippers jointly with the longer-period responses (cf. Munch et al,
229 2020) to constrain conductivity throughout the entire depth range. The reliability of the inversions in
230 particular depends on how accurate we represent in the model the oceanic conductivity. In this context
231 we believe it is worth effort to use depth-varying oceanic conductivity during inversions provided these
232 data are considered to be trustworthy.

233 **List of abbreviations**

234 EM: Electromagnetic;

235 1-D: one-dimensional;

236 2-D: two-dimensional;

237 3-D: three-dimensional;

238 OIE: Ocean Induction Effect;

239 GEBCO: General Bathymetry Chart of the Oceans;

240 MT: Magnetotellurics;

241 **Authors' contributions**

242 RR estimated tippers from observatory data, prepared 3-D conductivity models, performed 3-D modeling
243 and analyzed the results. MK provided the 3-D EM modeling code PGIEM2G and assisted RR with
244 the modeling. EM and MK provided the codes for converting global bathymetry/topography and ocean
245 conductivity data into 3-D conductivity models. AK created the concept of the study, and AK and KP
246 supervised the RR's work. JP prepared global oceanic conductivity data. JM obtained and provided
247 SHE and SMA magnetic field data. RR drafted the manuscript, and all authors read and approved the
248 final version.

249 **Authors' information**

250 ¹: Department of Geophysics, Observatório Nacional, Rio de Janeiro, Brazil. ²: Institute of Geophysics,
251 ETH Zürich, Zürich, Switzerland. ³: Geoelectromagnetic Research Center, Institute of Physics of the
252 Earth, Troitsk, Russia. ⁴: GFZ German Research Centre for Geosciences, Potsdam, Germany. ⁵: Institute
253 of Physics of the Earth, Moscow, Russia. ⁶: Geophysical Center, Moscow, Russia.

254 **Acknowledgments**

255 The authors acknowledge national institutes around the world that operate geomagnetic observatories,
256 and INTERMAGNET (www.intermagnet.org) which promotes high standards of observatory practice.
257 We also acknowledge the work of GEBCO group for providing publicly available global bathymetry
258 data.

259 **Availability of data and materials**

260 The results presented in this paper rely on 1 Hz data collected at geomagnetic observatories. These
261 data were digitally filtered to produce one minute means that are available from the INTERMAGNET
262 data repository.

263 **Competing interests**

264 The authors declare that they have no competing interests.

265 **Funding**

266 RR was supported by CNPq, Process 133345/2018-1. MK was supported by grant 20-05-00001 from the
267 Russian Foundation for Basic Research. AK was partially supported by the European Space Agency
268 through the Swarm DISC project. KP was supported by FAPERJ (Jovem Cientista do Nosso Estado,
269 Process 202.748/2019). EM was supported by grant 16-17-00121 from the Russian Science Foundation.
270 JP was supported by the German Research Foundation's priority program 1788 "Dynamic Earth".

271 **References**

- 272 Araya Vargas J., Ritter O. (2016) Source effects in mid-latitude geomagnetic transfer functions.
273 *Geophysics Journal International* 204(1):606–630
- 274 Aster R., Borchers B., Thurber C. (2005) Parameter estimation and inverse problems. Elsevier
275 Academic Press, Waltham(MA)
- 276 Banks R. J. (1969) Geomagnetic variations and the electrical conductivity of the upper mantle.
277 *Geophysics Journal International* 17(5):457–487
- 278 Bedrosian P. A., Feucht D. W. (2014) Structure and tectonics of the northwestern united states from
279 earthscope usarray magnetotelluric data. *Earth Planet Sci Lett* 402:275–289
- 280 Berdichevsky M. N., Dmitriev V. (2008) Models and methods of magnetotellurics. Springer, Berlin
- 281 Cabanes C., Grouazel A., von Schuckmann K., Hamon M., Turpin V., Coatanoan C. (2013) The cora
282 dataset: Validation and diagnostics of in-situ ocean temperature and salinity measurements. *Ocean*
283 *Science* 9(1):1–18
- 284 Chen C., Kruglyakov M., Kuvshinov A. (2020) A new method for accurate and efficient modeling of the
285 local ocean induction effects. Application to long-period responses from island geomagnetic

286 observatories. *Geophysical Research Letters* 47(8):e2019GL086,351, DOI 10.1029/2019GL086351

287 GEBCO (2019) Gebco compilation group (2019) gebco 2019 grid.

288 doi:105285/836f016a-33be-6ddc-e053-6c86abc0788e

289 Grayver A. V., Kolev T. (2015) Large-scale 3d geo-electromagnetic modeling using parallel adaptive

290 high-order finite element method. *Geophysics* 80(6):277–291

291 Grayver A. V., Munch F. D., Kuvshinov A. V., Khan A., Sabaka T. J., Tøffner-Clausen L. (2017) Joint

292 inversion of satellite-detected tidal and magnetospheric signals constrains electrical conductivity and

293 water content of the upper mantle and transition zone. *Geophysical Research Letters*

294 44(12):6074–6081

295 Kelbert A., Schultz A., Egbert G. (2009) Global electromagnetic induction constraints on

296 transition-zone water content variations. *Nature* 460:1003–1007

297 Koyama T., Khan A., Kuvshinov A. (2014) Three-dimensional electrical conductivity structure beneath

298 Australia from inversion of geomagnetic observatory data: evidence for lateral variations in

299 transition-zone temperature, water content and melt. *Geophys J Int* 196:1330–1350,

300 DOI 10.1093/gji/ggt455

301 Kruglyakov M., Kuvshinov A. (2018) Using high-order polynomial basis in 3-d em forward modeling

302 based on volume integral equation method. *Geophys J Int* 213:1387–1401

303 Li S., Weng A., Zhang Y., Schultz A., Li Y., Tang Y., Zou Z., Zhou Z. (2020) Evidence of Bermuda hot

304 and wet upwelling from novel three-dimensional global mantle electrical conductivity image.

305 *Geochemistry, Geophysics, Geosystems* 21(6), DOI 10.1029/2020GC009016

306 Marcuello A., Queralt P., Ledo J. (2005) Applications of dispersion relations to the geomagnetic

307 transfer function. *Physics of the Earth and Planetary Interiors* 150:85–91

308 Morschhauser A., Grayver A. V., Kuvshinov A. V., Samrock F., Matzka J. (2019) Tippers at island

309 geomagnetic observatories constrain electrical conductivity of oceanic lithosphere and upper mantle.

310 *Earth, Planets and Space* 71(1):17

311 Munch F. D., Grayver A. V., Kuvshinov A., Khan A. (2018) Stochastic inversion of geomagnetic

312 observatory data including rigorous treatment of the ocean induction effects with implications for

313 transition zone water content and thermal structure. *Journal of Geophysical Research* 123:31–51

314 Munch F. D., Grayver A. V., Guzavina M., Kuvshinov A., Khan A. (2020) Joint inversion of daily and

315 long-period transfer functions reveals lateral variations in mantle water content. *Geophys Res Lett*

316 47, DOI e2020GL087222. <https://doi.org/10.1029/2020GL087222>

317 Olsen N. (1998) The electrical conductivity of the mantle beneath europe derived from c-responses from
318 3 to 720 hr. *Geophys J Int* 133(2):298–308

319 Pankratov O., Avdeev D., Kuvshinov A. (1995) Electromagnetic field scattering in a heterogeneous
320 earth: A solution to the forward problem. *Izvestiya, Physics of the Solid Earth* 31(3):201–209

321 Parkinson W., Jones F. W. (1979) The geomagnetic coast effect. *Reviews of Geophysics and Space*
322 *Physics* 17(8):1999–2017

323 Petereit J., Saynisch-Wagner J., Irrgang C., Thomas M. (2019) Analysis of ocean-tide induced magnetic
324 fields derived from oceanic in situ observations: Climate trends and the remarkable sensitivity of shelf
325 regions. *Journal of Geophysical Research: Oceans* 124:8257–8270

326 Pütke C., Kuvshinov A. (2014) Mapping 3-d mantle electrical conductivity from space: a new 3-d
327 inversion scheme based on analysis of matrix q-responses. *Geophysical Journal International*
328 197(2):768–784

329 Rao C. K., Jones A. G., Moorkamp M., Weckmann U. (2014) Implications for the lithospheric geometry
330 of the iapetus suture beneath ireland based on electrical resistivity models from deep-probing
331 magnetotellurics. *Geophys J Int* 198:737–759

332 Samrock F., Kuvshinov A. (2013) Tipper at island observatories: Can we use them to probe electrical
333 conductivity of the earth’s crust and upper mantle? *Geophysical Research Letters* 40:824–828

334 Semenov A., Kuvshinov A. (2012) Global 3-D imaging of mantle electrical conductivity based on
335 inversion of observatory C-responses – II. Data analysis and results. 191:965–992

336 Singer B. (1995) Method for solution of maxwell’s equations in non-uniform media. *Geophysical Journal*
337 *International* 120:590–598

338 Straume E. O., Gaina C., Medvedev S., Hochmuth K., Gohl K., Whittaker J. M., Absul Fattah R.,
339 Doornenbal J. C., Hopper J. R. (2019) Globsed: Updated total sediments thickness in the world’s
340 oceans. *Geochemistry, Geophysics, Geosystems* 20:<https://doi.org/10.1029/2018GC008115>

341 Sun J., Kelbert A., Egbert G. D. (2015) Ionospheric current source modeling and global geomagnetic
342 induction using ground geomagnetic observatory data. *J Geophys Res Solid Earth* 120:6771–6796,
343 DOI 10.1002/2015JB012063

344 Tietze K., Ritter O. (2013) Three-dimensional magnetotelluric inversion in practice—the electrical
345 conductivity structure of the san andreas fault in central california. *Geophys J Int* 195:130–147

346 Tyler R. H., Boyer T. P., Minami T., Zweng M. M., Reagan J. R. (2017) Electrical conductivity of the
347 global ocean. *Earth, Planets and Space* 69:156–166

348 Utada H., Koyama T., Shimizu H., Chave A. D. (2003) A semi-global reference model for electrical
349 conductivity in the mid-mantle beneath the north pacific region. *Geophysical Research Letters*
350 30(4):1194–1198

351 Weidelt P. (1972) The inverse problem of geomagnetic induction, z. *Geophysics* 38:257–289

352 Yang B., Egbert G. D., Kelbert A., N. M. (2015) Three-dimensional electrical resistivity of the
353 north-central usa from earthscope long period magnetotelluric data. *Earth Planet Sci Lett* 422:87–93

354 Zhang Y., Weng A., Li S., Yang Y., Tang Y., Liu Y. (2020) Electrical conductivity in the mantle
355 transition zone beneath Eastern China derived from L1-Norm C-responses. *Geophysical Journal
356 International* 221(2):1110–1124, DOI 10.1093/gji/ggaa059

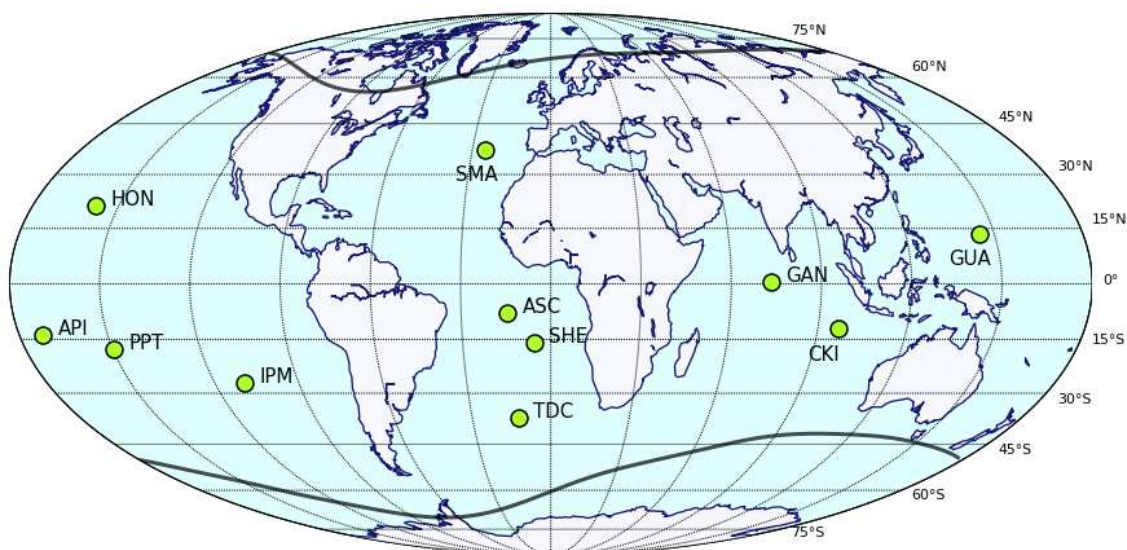


Figure 1. : Location of geomagnetic observatories used in this study (green dots). Black lines depict $\pm 55^\circ$ quasi dipole latitudes. Relevant information about these observatories is summarized in Table 1.

Table 1. : Information on the geomagnetic observatories used in this study. From left to right: IAGA code, observatory name, geographic and geomagnetic latitude and longitude, and time interval used to estimate tippers. Observatories with an asterisk (*) are, as of date, not participating in INTERMAGNET and data is available from GFZ Potsdam. Geomagnetic coordinates were calculated using the IGRF-12 model, epoch 2015.

Code	Name	lat^{GG}	lon^{GG}	lat^{GM}	lon^{GM}	Time interval used for tippers' estimation
API	Apia	-13.81	-171.78	-15.05	263.35	01/01/2016 – 31/12/2017
ASC	Ascension Island	-7.95	-14.38	-2.77	57.48	01/01/2014 – 31/12/2015
CKI	Cocos-Keeling Islands	-12.10	96.84	-21.56	168.92	01/01/2017 – 31/12/2018
GAN	Gan	0.69	73.15	-8.64	145.33	01/01/2016 – 31/12/2017
GUA	Guam	13.59	144.87	5.8	216.51	01/01/2017 – 31/12/2018
HON	Honolulu	20.32	-158	21.65	270.85	01/01/2015 – 31/12/2016
IPM	Easter Island	-27.2	-109.42	-19.17	325.61	01/01/2013 – 31/12/2015
PPT	Pamatai	-17.57	-149.58	-15.05	285.79	01/01/2015 – 31/12/2016
SHE	St. Helena*	-15.90	-5.75	11.78	64.24	01/01/2015 – 31/12/2015
SMA	Santa Maria/Azores*	36.99	-25.13	43.21	53.57	01/05/2018 – 31/09/2019
TDC	Tristan da Cunha	-37.07	-12.31	-31.70	54.76	01/01/2013 – 31/12/2014

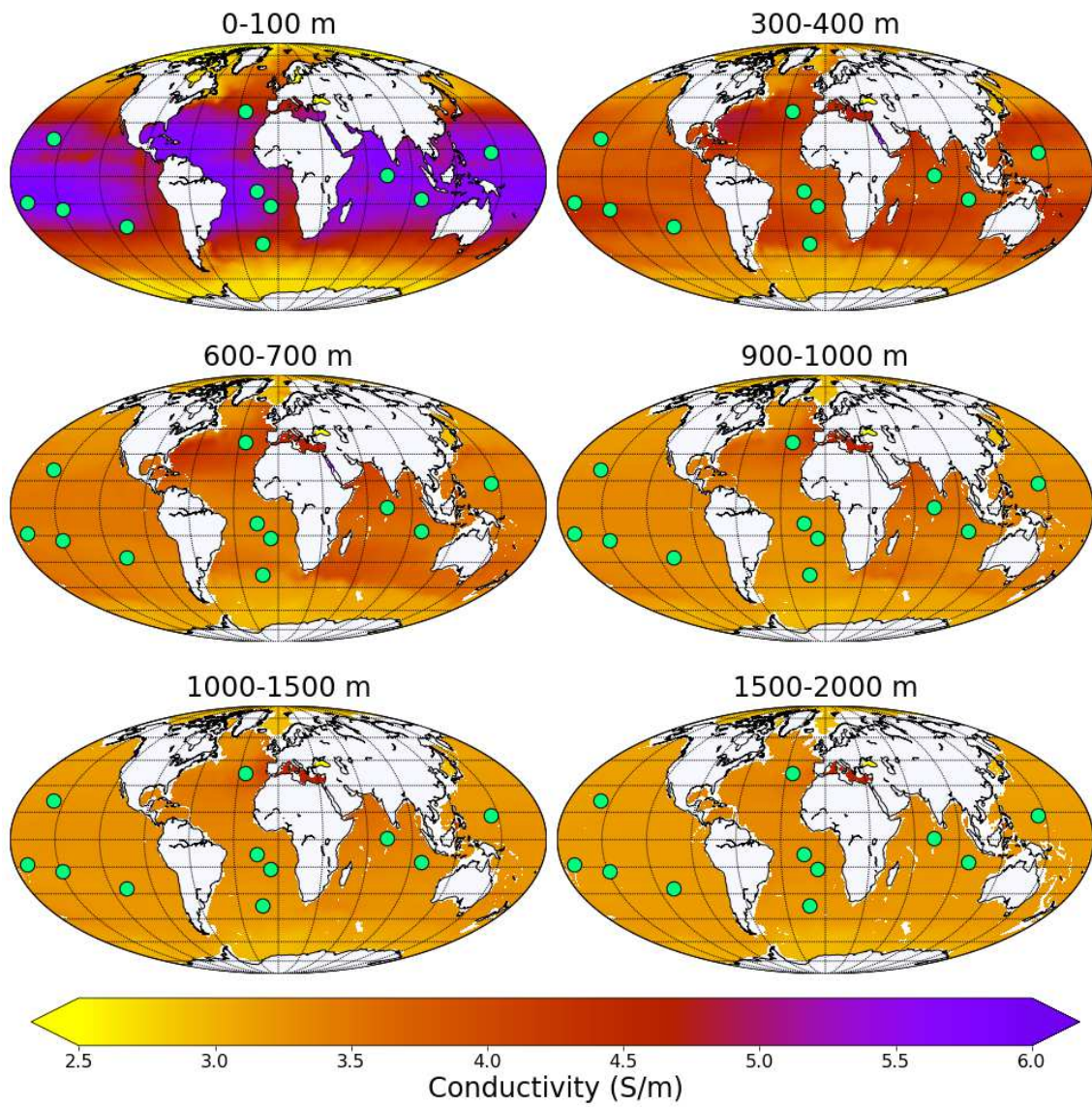


Figure 2. : Global maps of oceanic electric conductivity for six selected depth intervals for December 2015 model. Green dots denote the locations of the geomagnetic observatories used in this study.

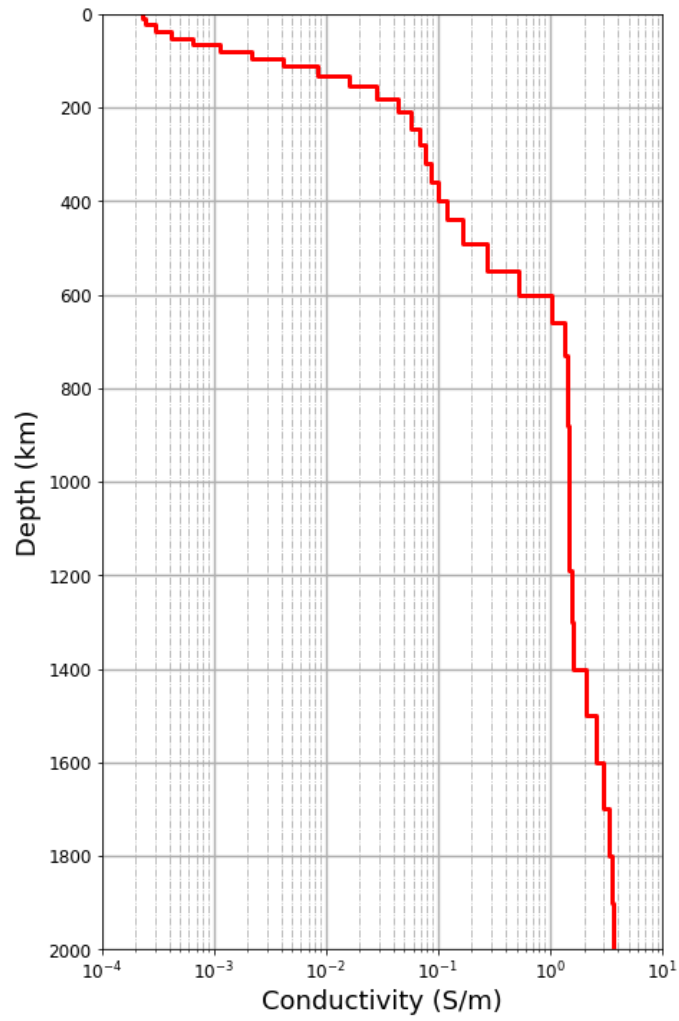


Figure 3. : 1-D global conductivity profile (from Grayver et al, 2017) used in this study for the crust and mantle beneath the 3-D (oceanic) modeling domains.

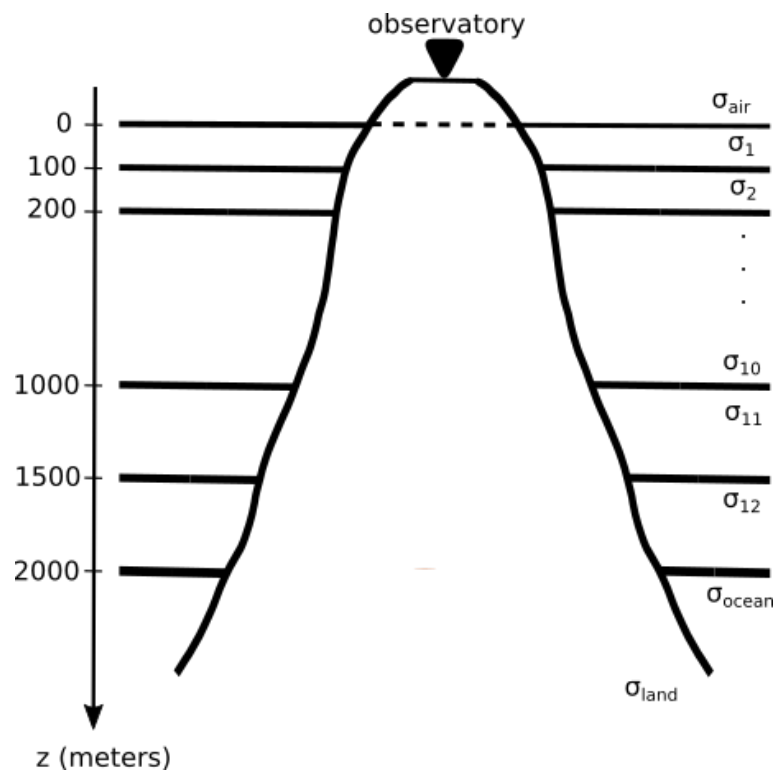


Figure 4. : Vertical parametrization of the oceanic conductivity distribution in the 3-D modeling domain. σ_1 to σ_{12} is the respective water layer's conductivity, set to the layer's average conductivity calculated from the global ocean conductivity model. σ_{ocean} is the deep (below 2000 m) ocean conductivity, which is set to 3.2 S/m. σ_{land} and σ_{air} are the landmass and air conductivity set to 0.01 S/m and 10^{-8} S/m, respectively.

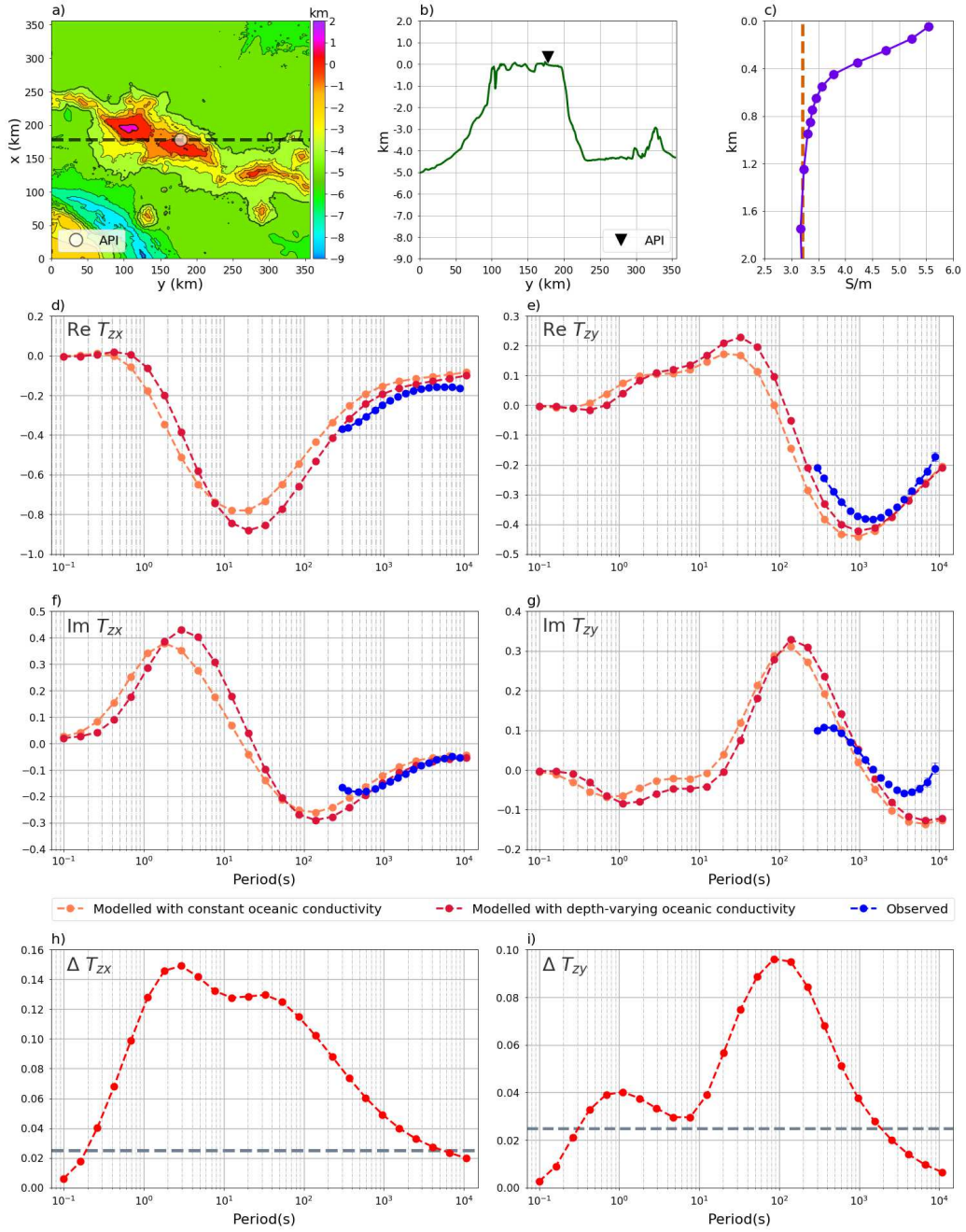


Figure 5. : Results for Apia observatory (API). (a) Map of bathymetry/topography; dashed line indicates location of profile shown in panel (b). (b) West-East oriented bathymetry profile. (c) Regional depth-varying (purple) oceanic conductivity and constant reference oceanic conductivity (3.2 S/m, orange dashed line). (d) to (g) Real and imaginary parts for x and y components of tippers computed in the model with depth-varying (orange dots and dashed line) and depth-constant (red dots and dashed line) oceanic conductivity. (h) Difference for the computed tipper x component between depth-varying and depth-constant ocean conductivity, see text for details. Dashed grey line indicates the threshold of 0.025. (i) Same as (h), but for the y component.

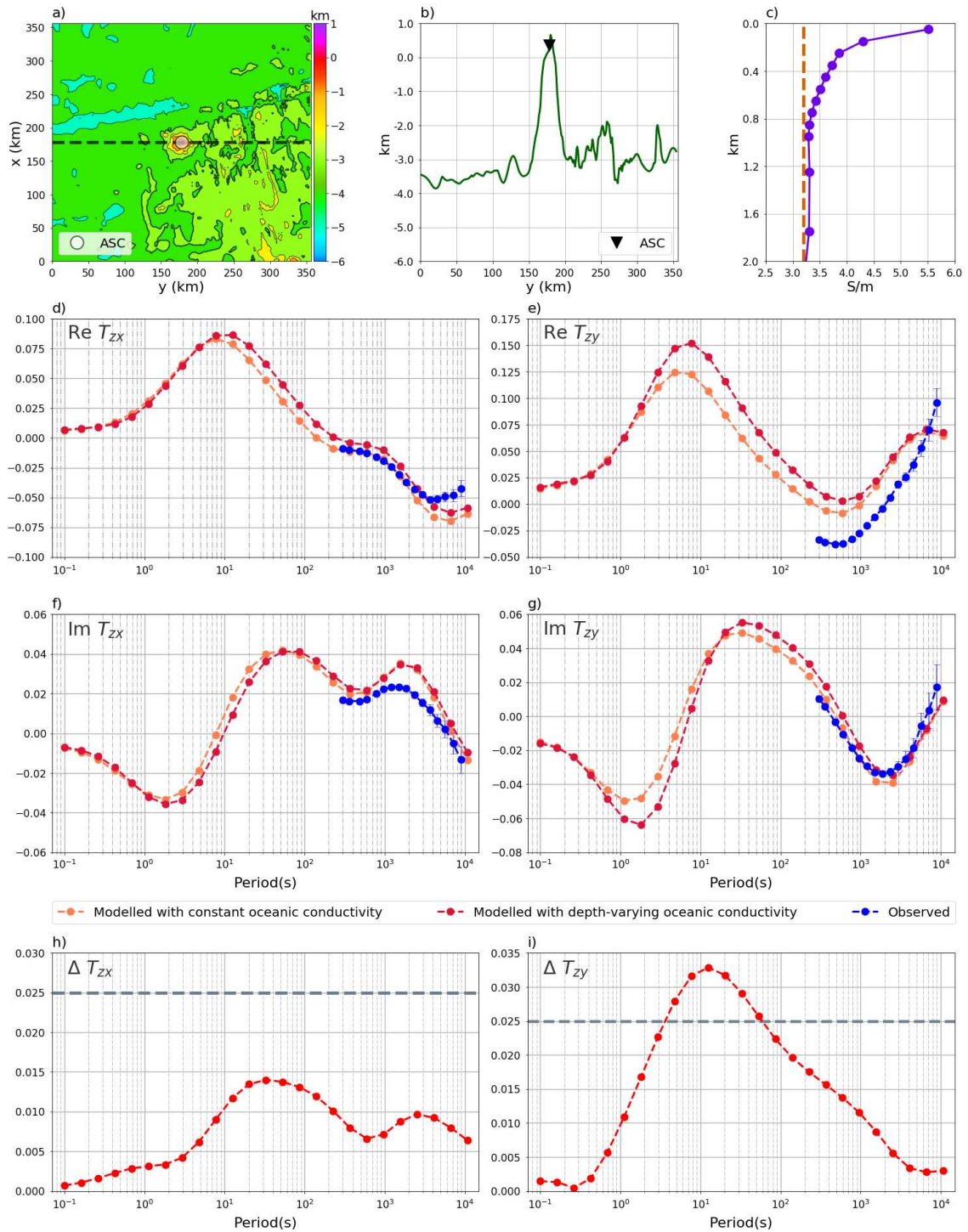


Figure 6. : Same as Figure 5, but for Ascension Island observatory (ASC).

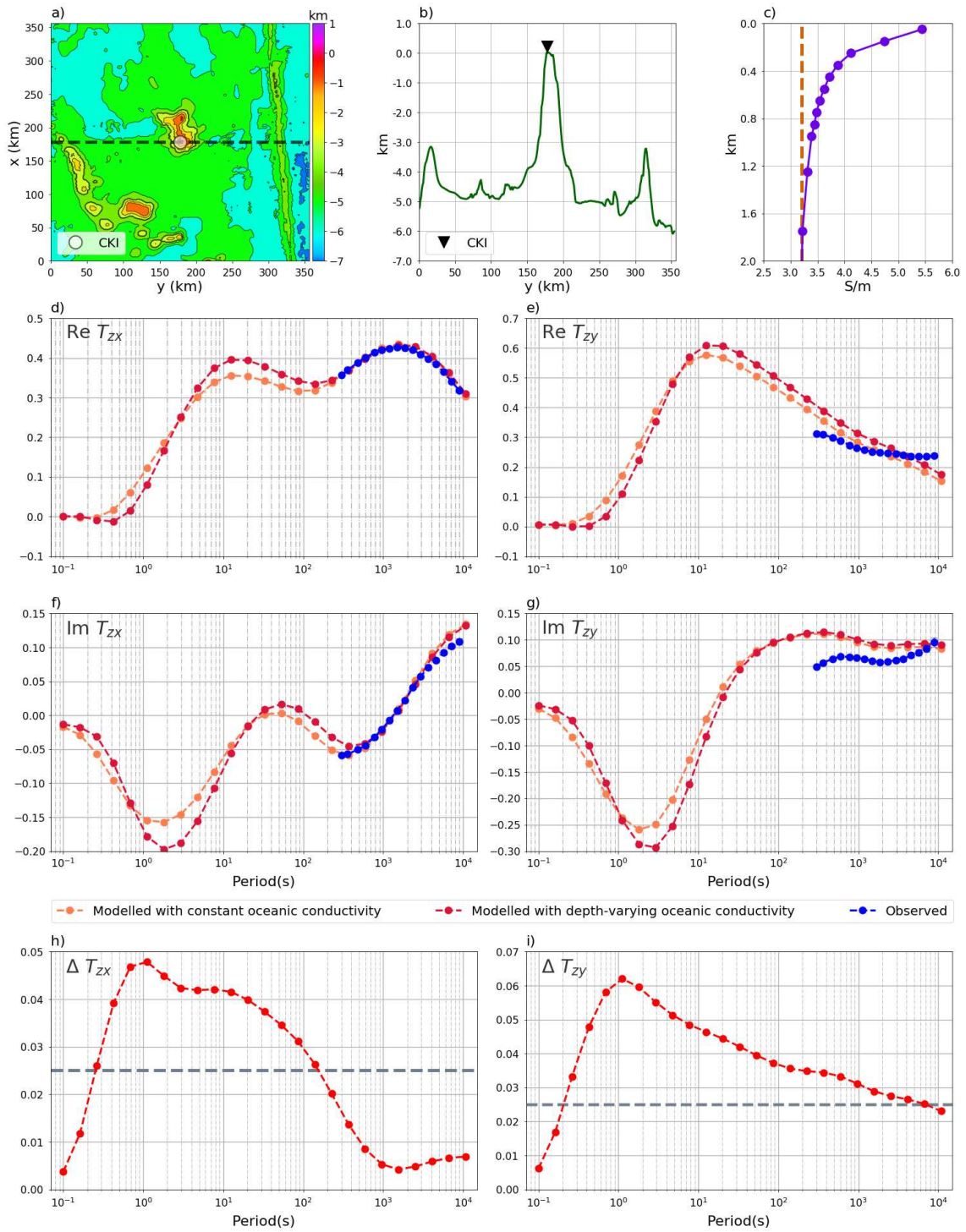


Figure 7. : Same as Figure 5, but for Cocos-Keeling Islands observatory (CKI).

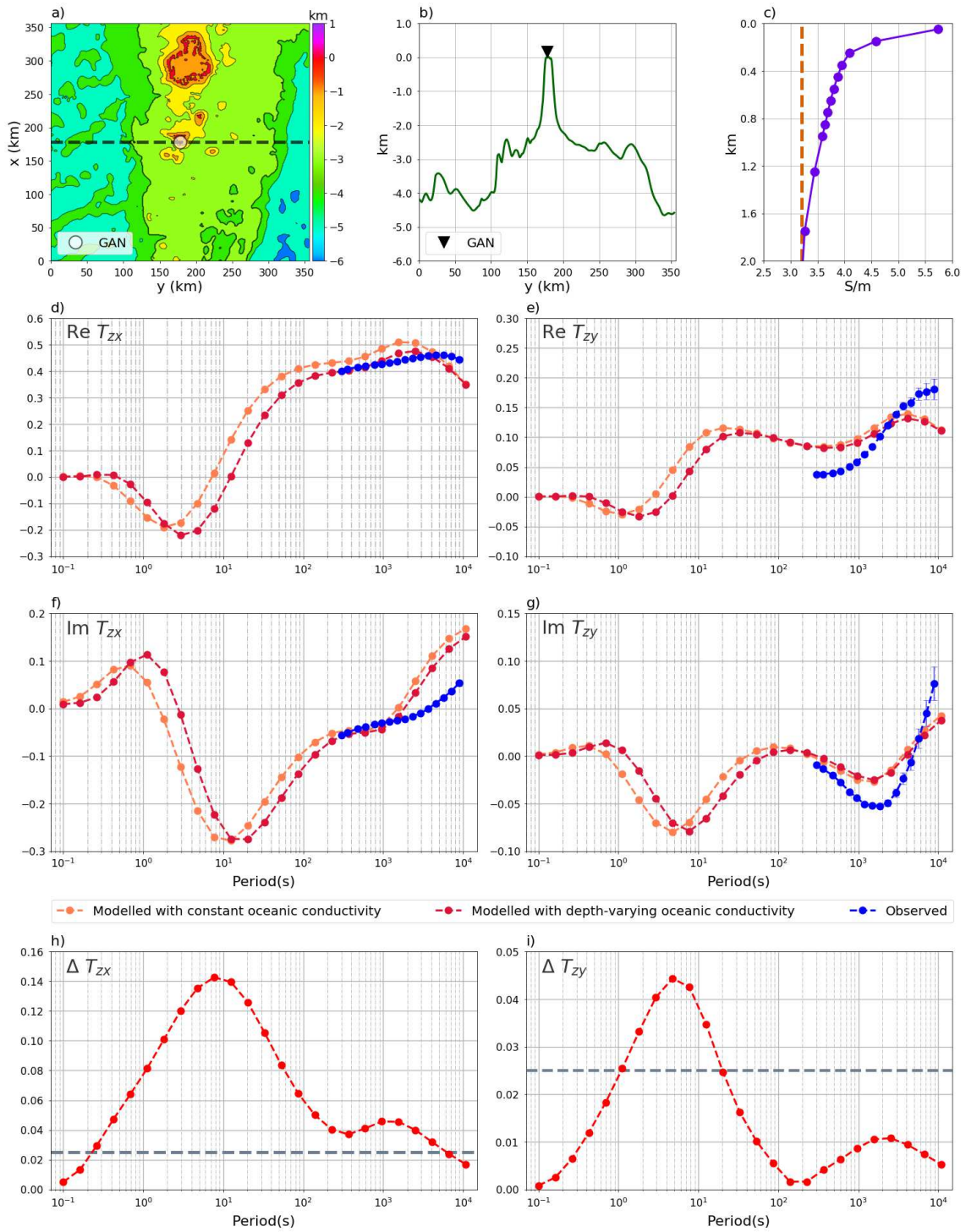


Figure 8. : Same as Figure 5, but for Gan observatory (GAN).

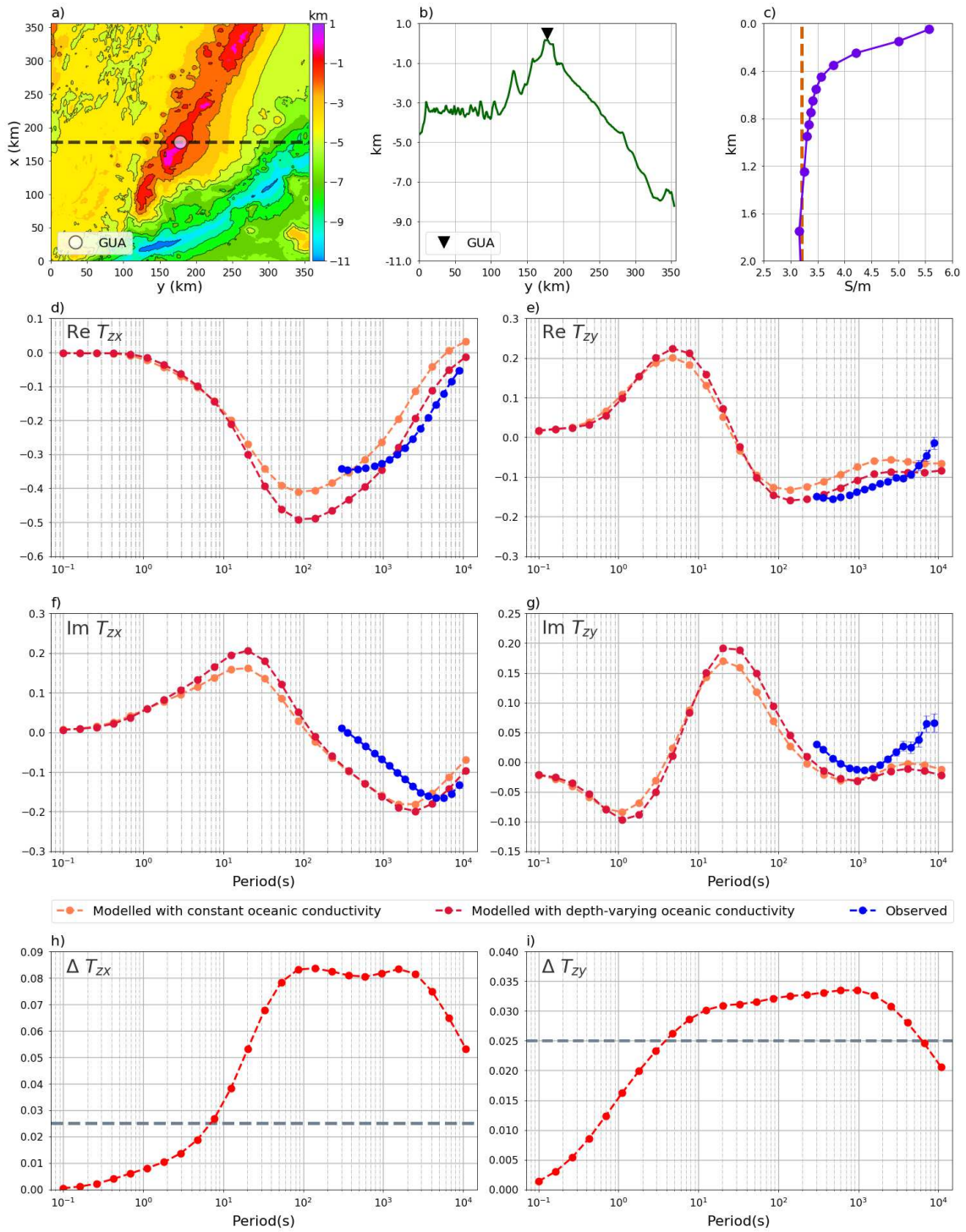


Figure 9. : Same as Figure 5, but for Guam observatory (GUA).

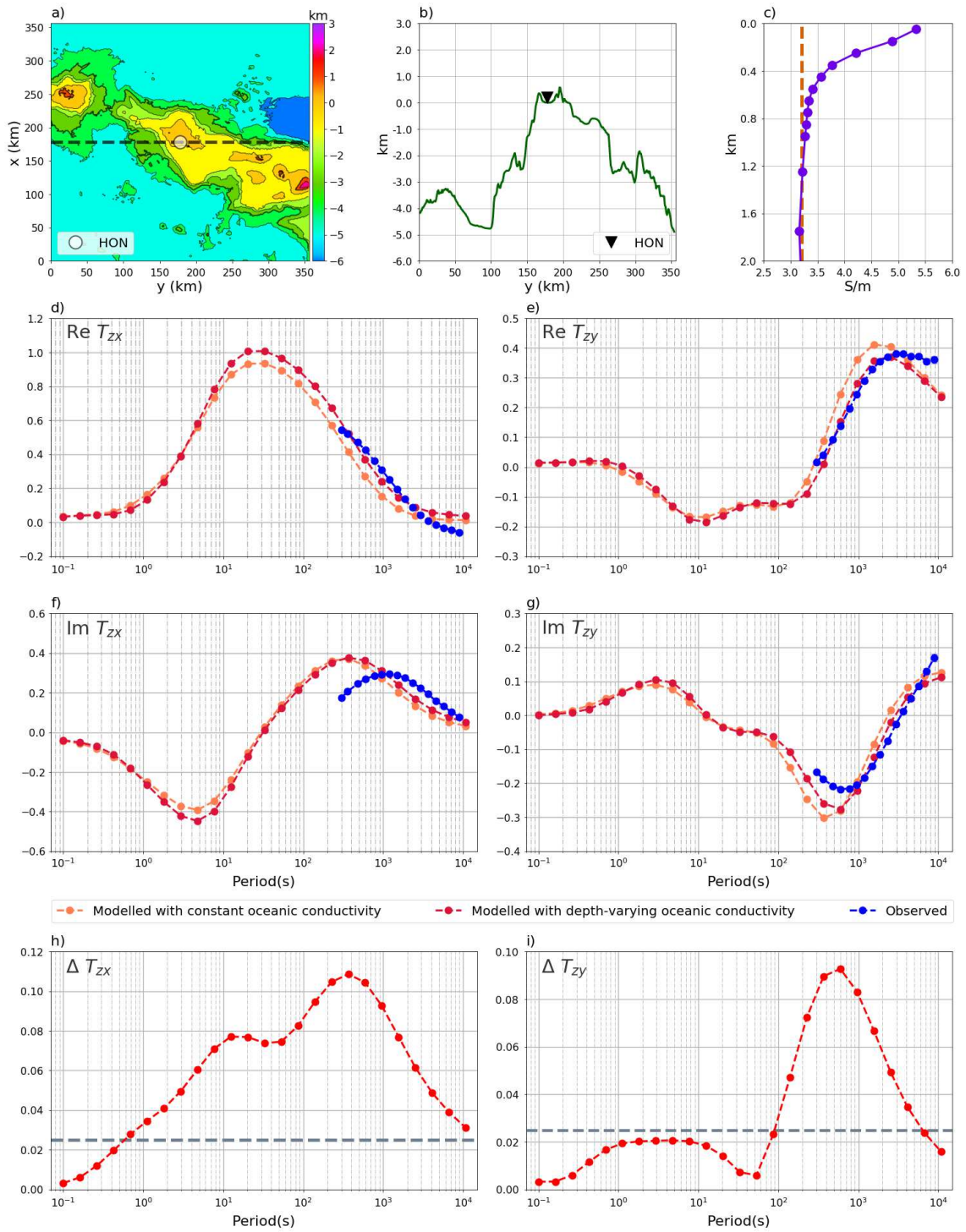


Figure 10. : Same as Figure 5, but for Honolulu observatory (HON).

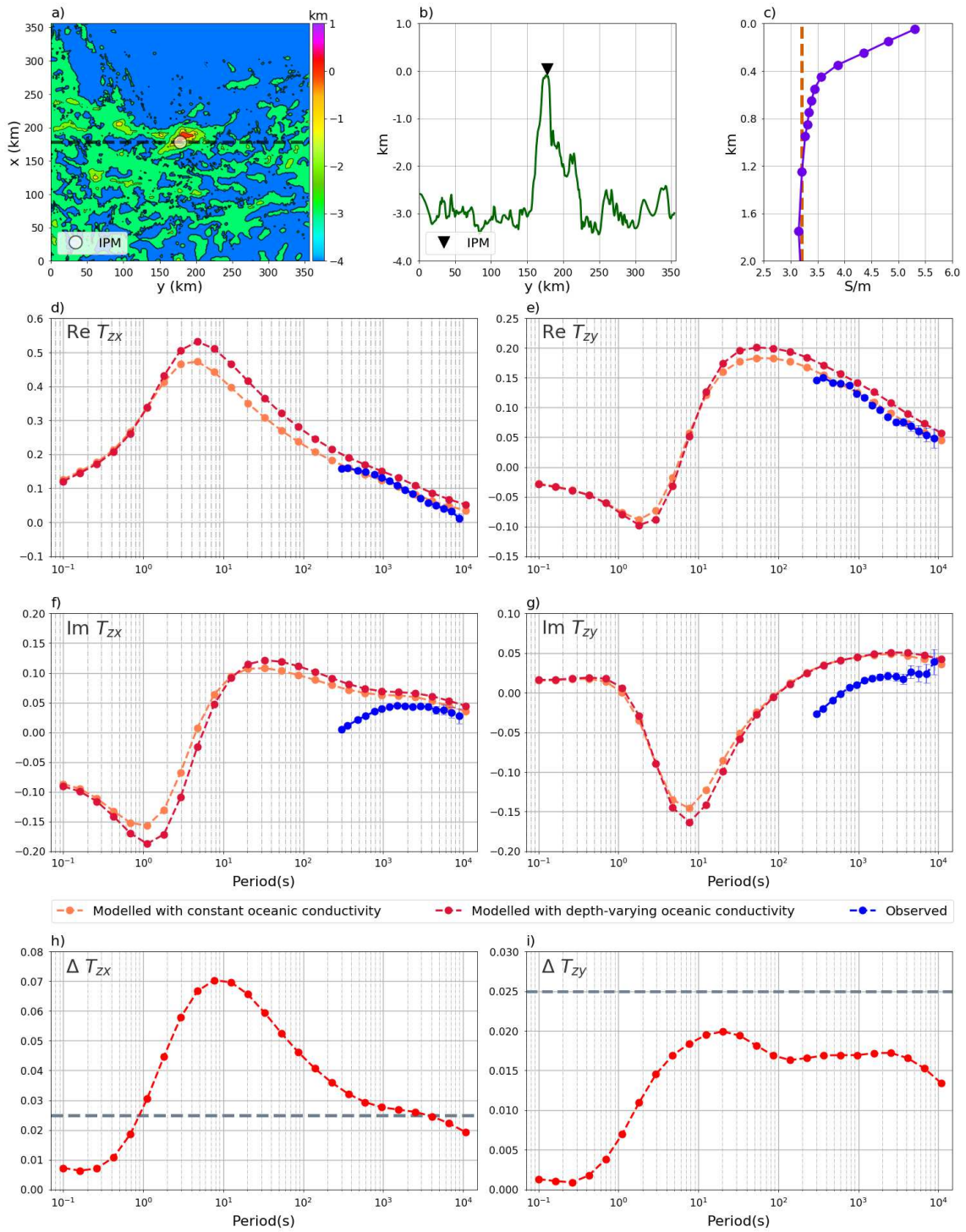


Figure 11. : Same as Figure 5, but for Easter Island observatory (IPM).

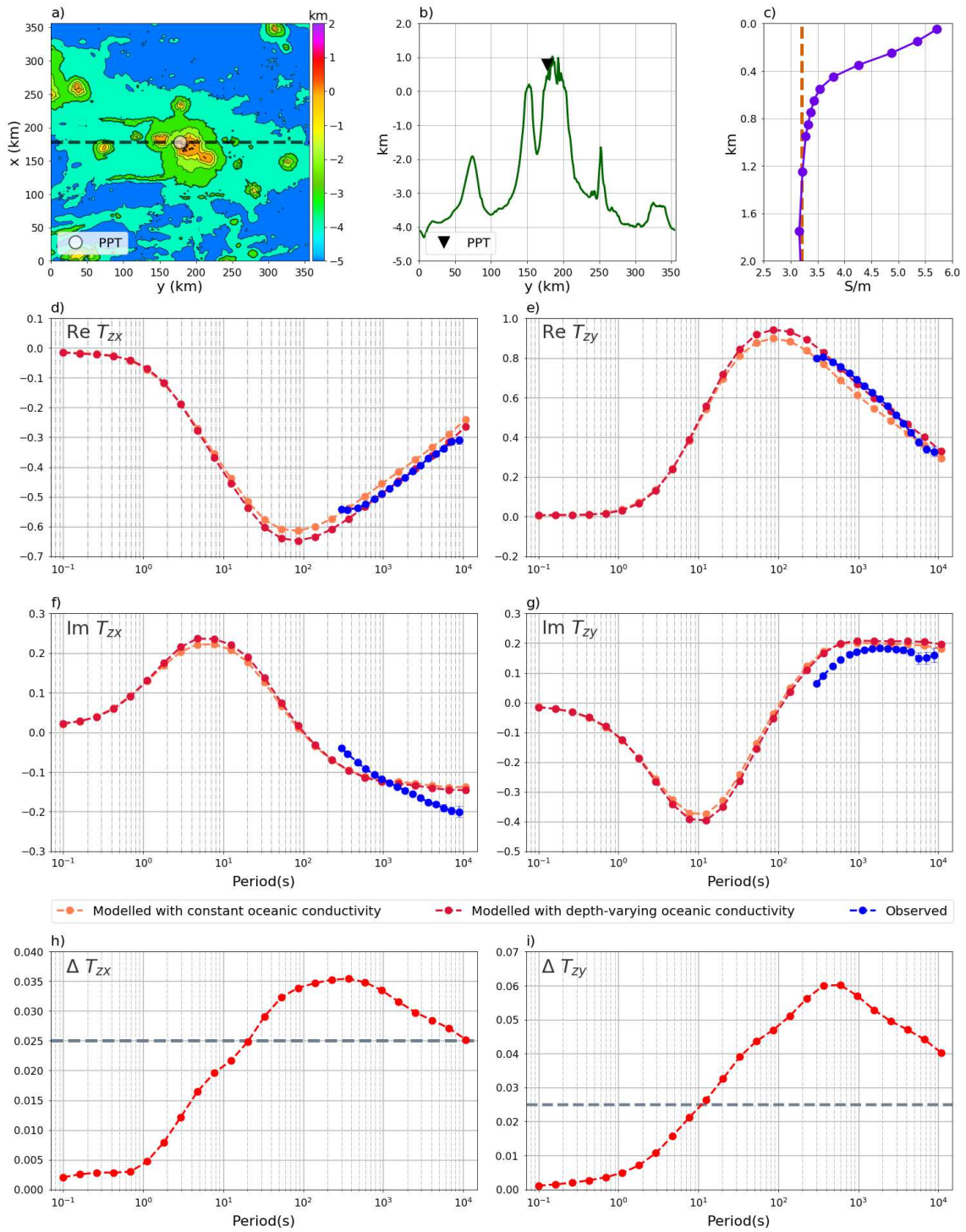


Figure 12. : Same as Figure 5, but for Pamatai observatory (PPT).

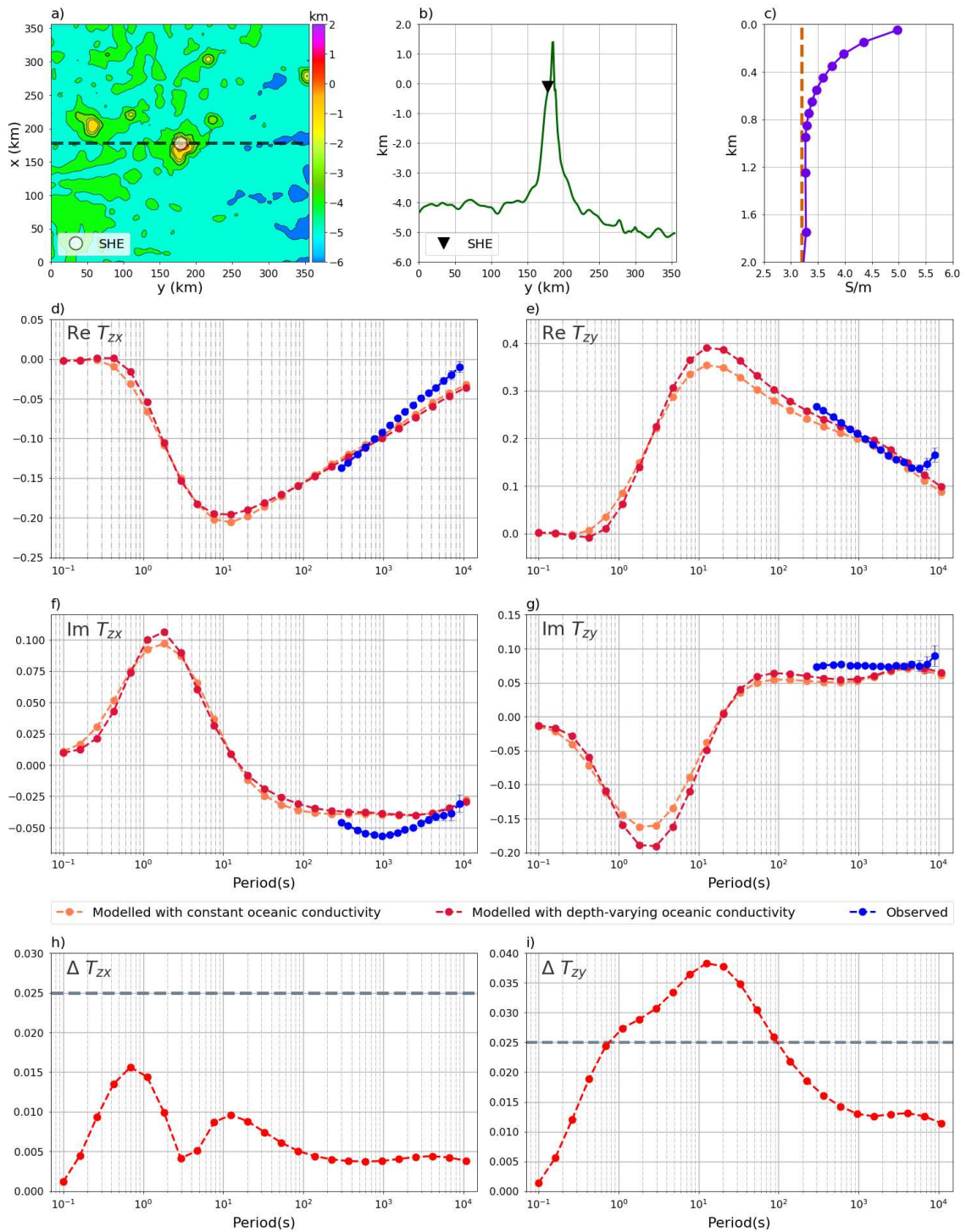


Figure 13. : Same as Figure 5, but for St. Helena observatory (SHE).

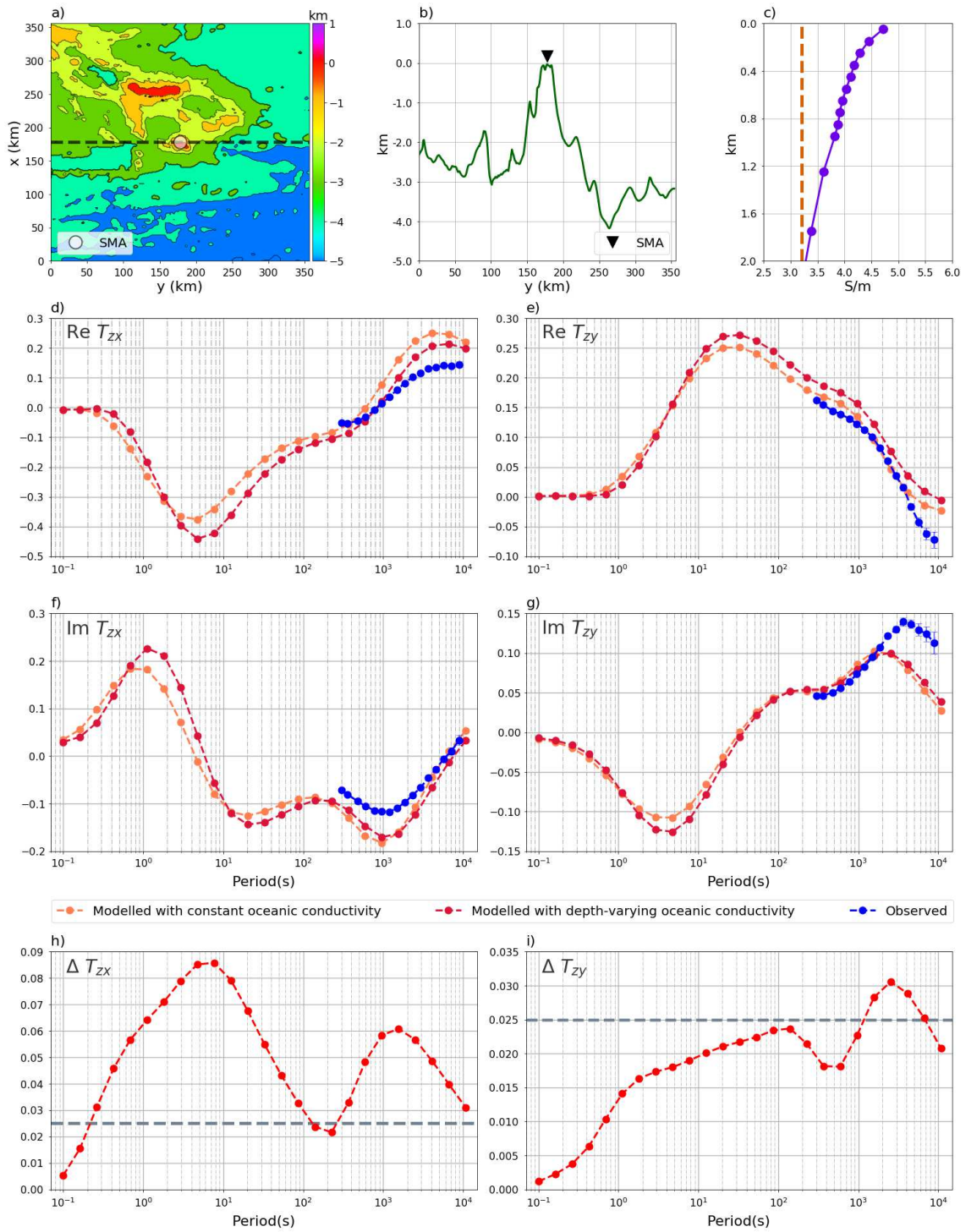


Figure 14. : Same as Figure 5, but for Santa-Maria/Azores observatory (SMA).

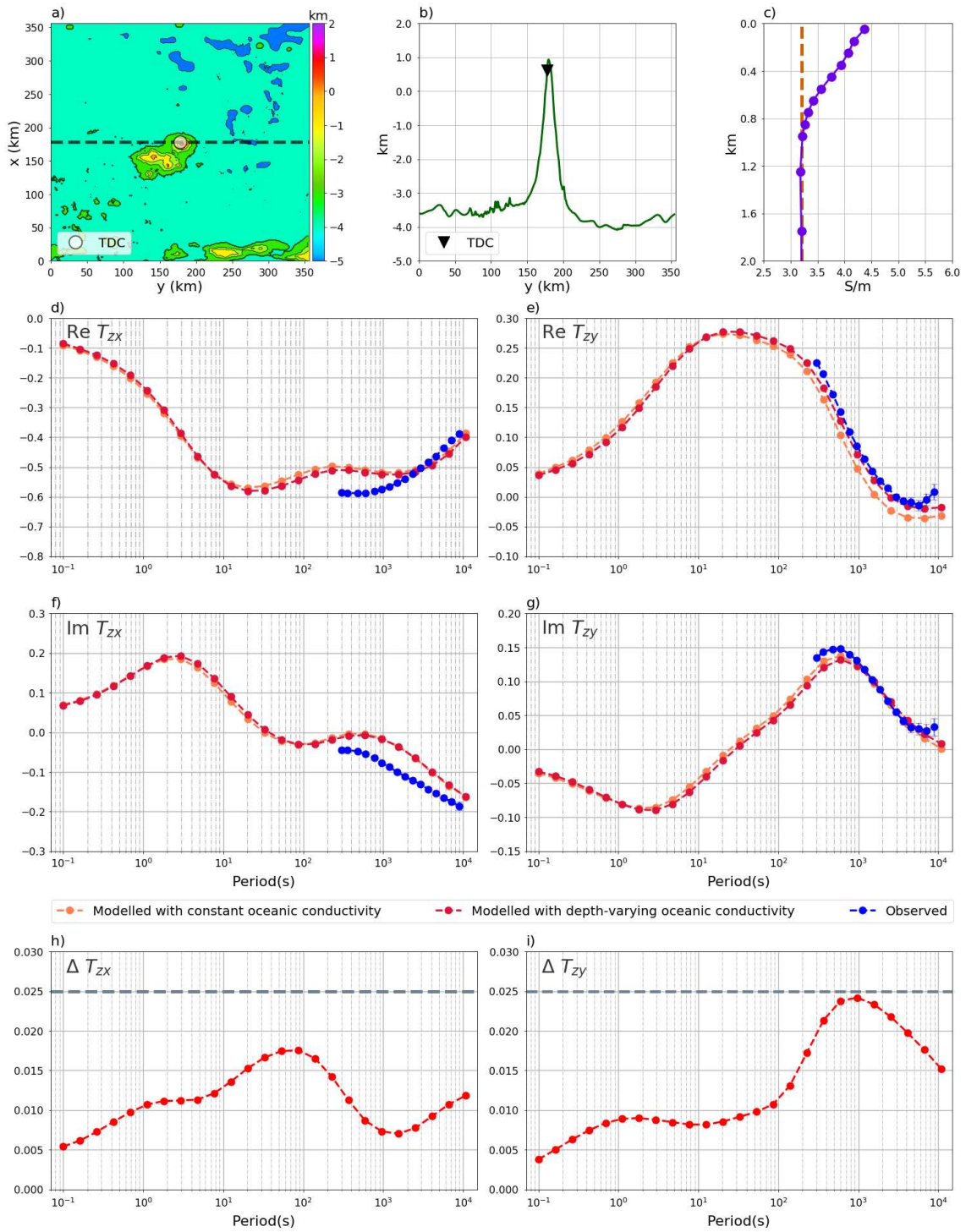


Figure 15. : Same as Figure 5, but for Tristan da Cunha observatory (TDC).

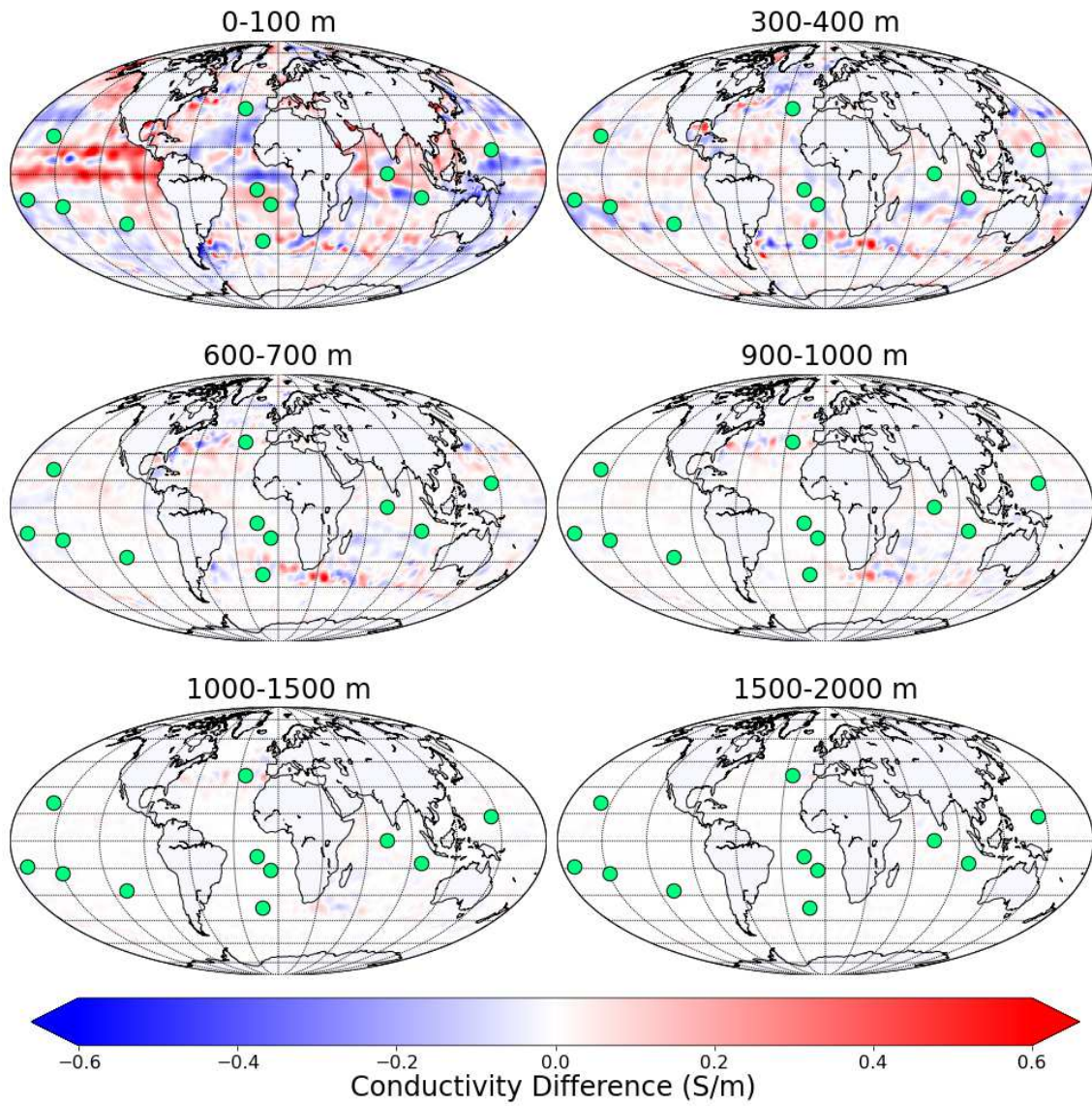


Figure 16. : Global maps of difference between 2015 December and June oceanic conductivity models at six depth intervals. Green circles denote locations of geomagnetic observatories used in this study.

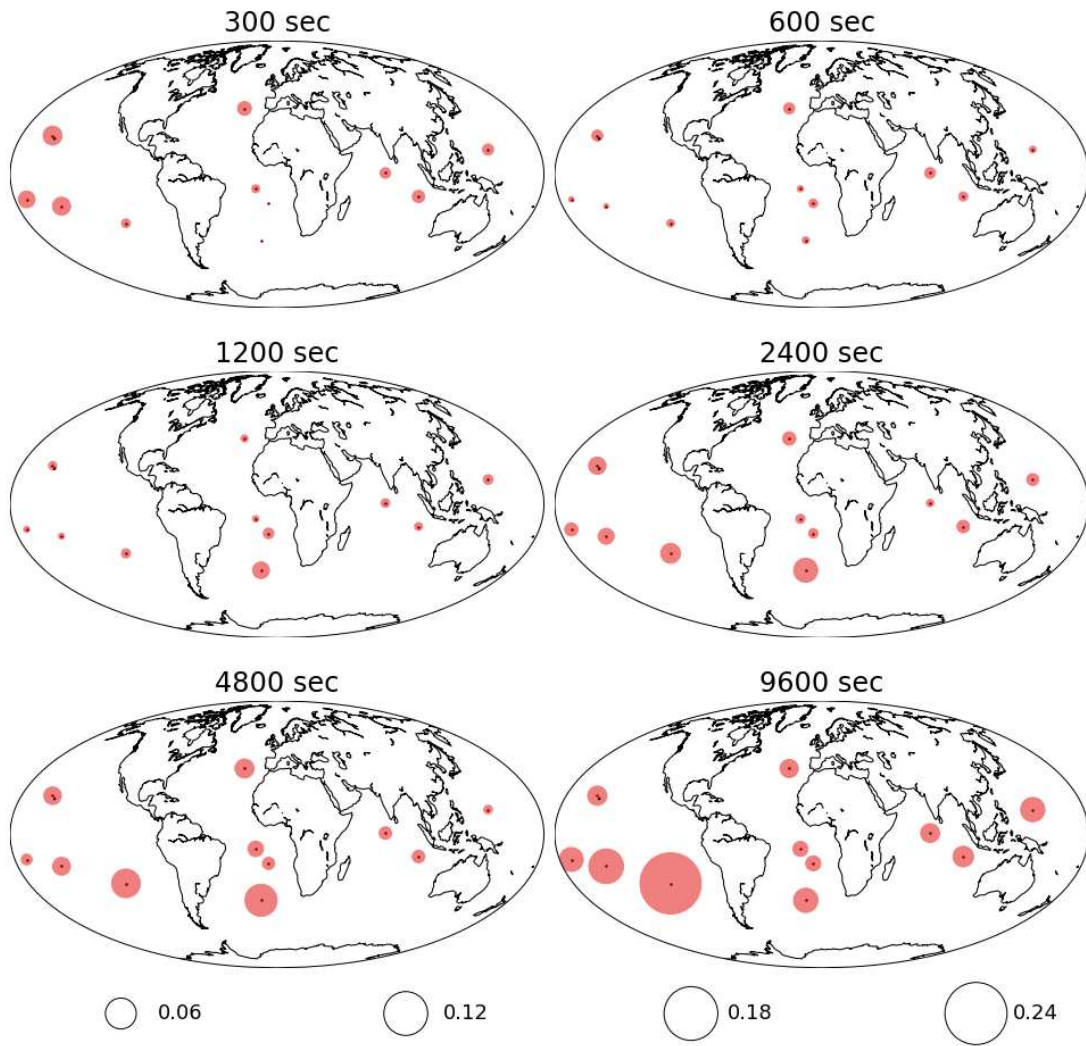


Figure 17. : Difference between “December” and “June” T_{zx} at island observatories, shown as filled circles. “Experimental” and “modeled” differences are colored by light and dark red, respectively. The size of circles below the plots indicates four ranges of differences.

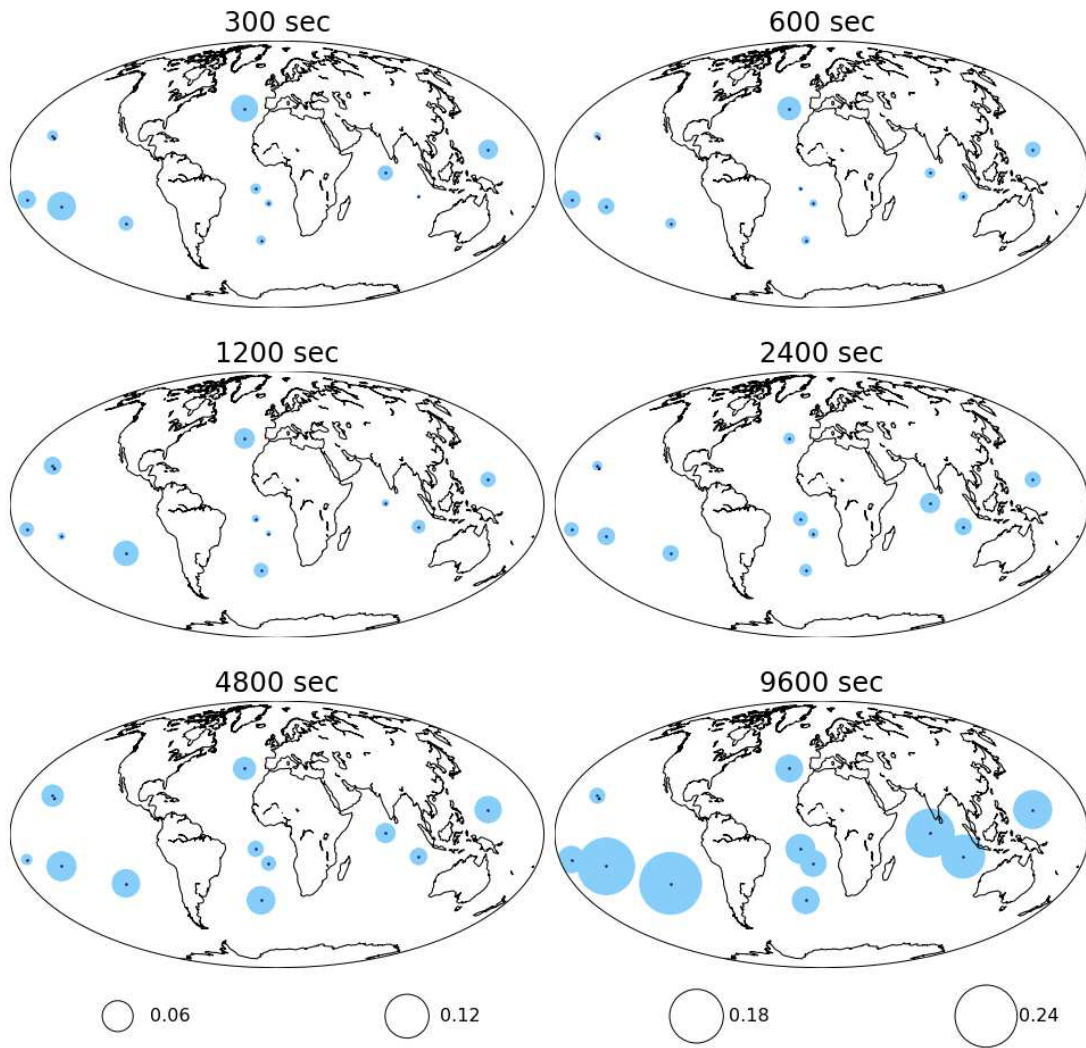


Figure 18. : Difference between “December” and “June” T_{zy} at island observatories, shown as filled circles. “Experimental” and “modeled” differences are colored by light and dark blue, respectively. The size of circles below the plots indicates four ranges of differences.

Figures

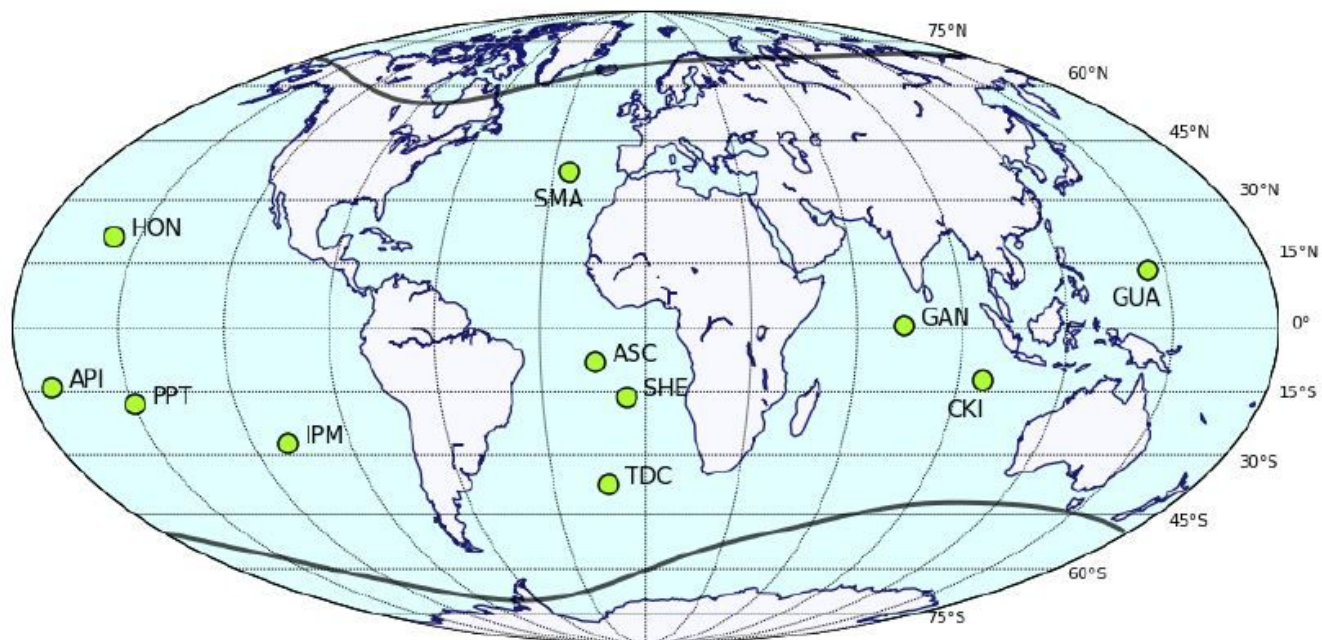


Figure 1

Location of geomagnetic observatories used in this study (green dots). Black lines depict ± 55 quasi dipole latitudes. Relevant information about these observatories is summarized in Table 1. Note: The designations employed and the presentation of the material on this map do not imply the expression of any opinion whatsoever on the part of Research Square concerning the legal status of any country, territory, city or area or of its authorities, or concerning the delimitation of its frontiers or boundaries. This map has been provided by the authors.

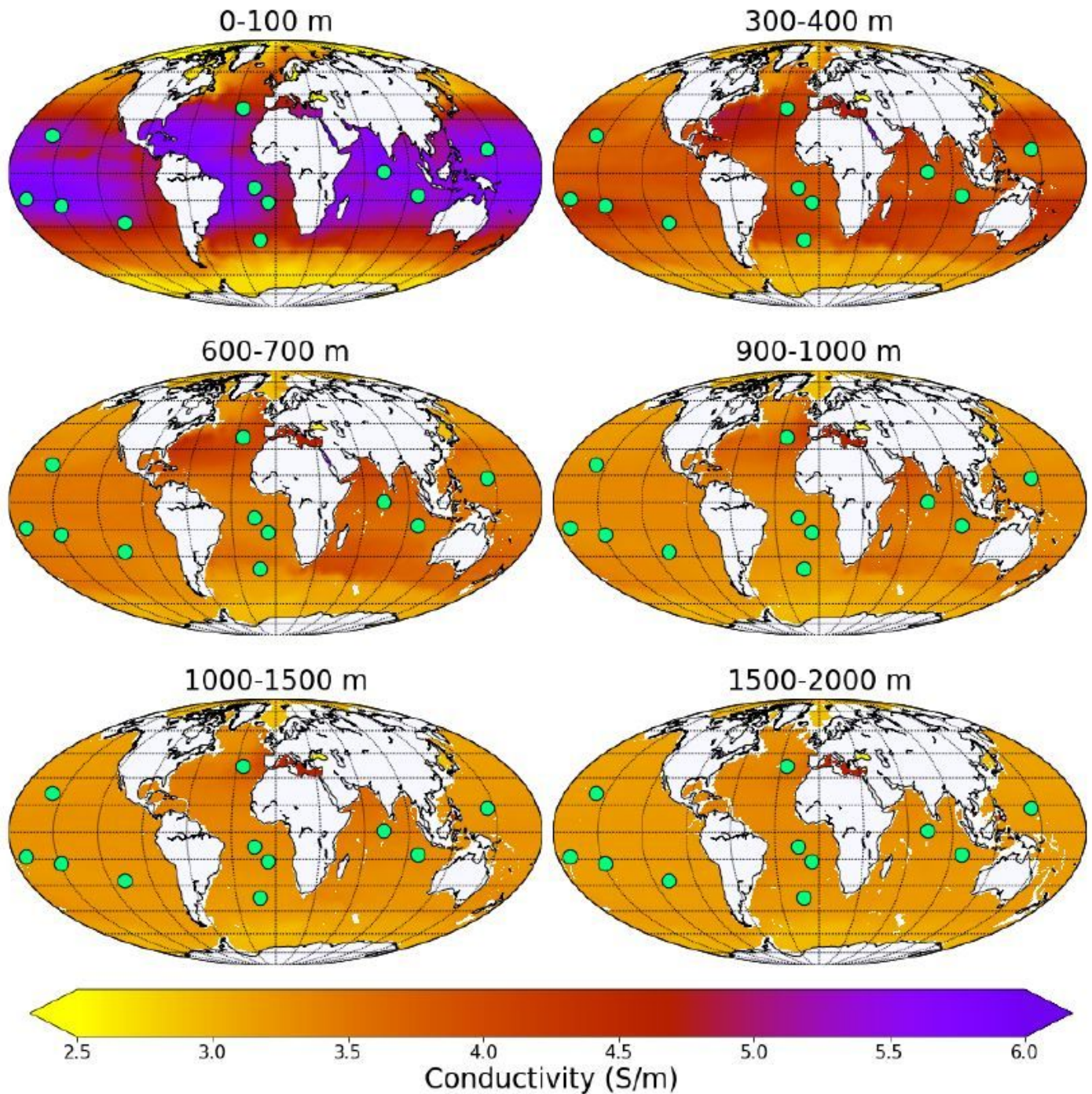


Figure 2

Global maps of oceanic electric conductivity for six selected depth intervals for December 2015 model. Green dots denote the locations of the geomagnetic observatories used in this study. Note: The designations employed and the presentation of the material on this map do not imply the expression of any opinion whatsoever on the part of Research Square concerning the legal status of any country, territory, city or area or of its authorities, or concerning the delimitation of its frontiers or boundaries. This map has been provided by the authors.

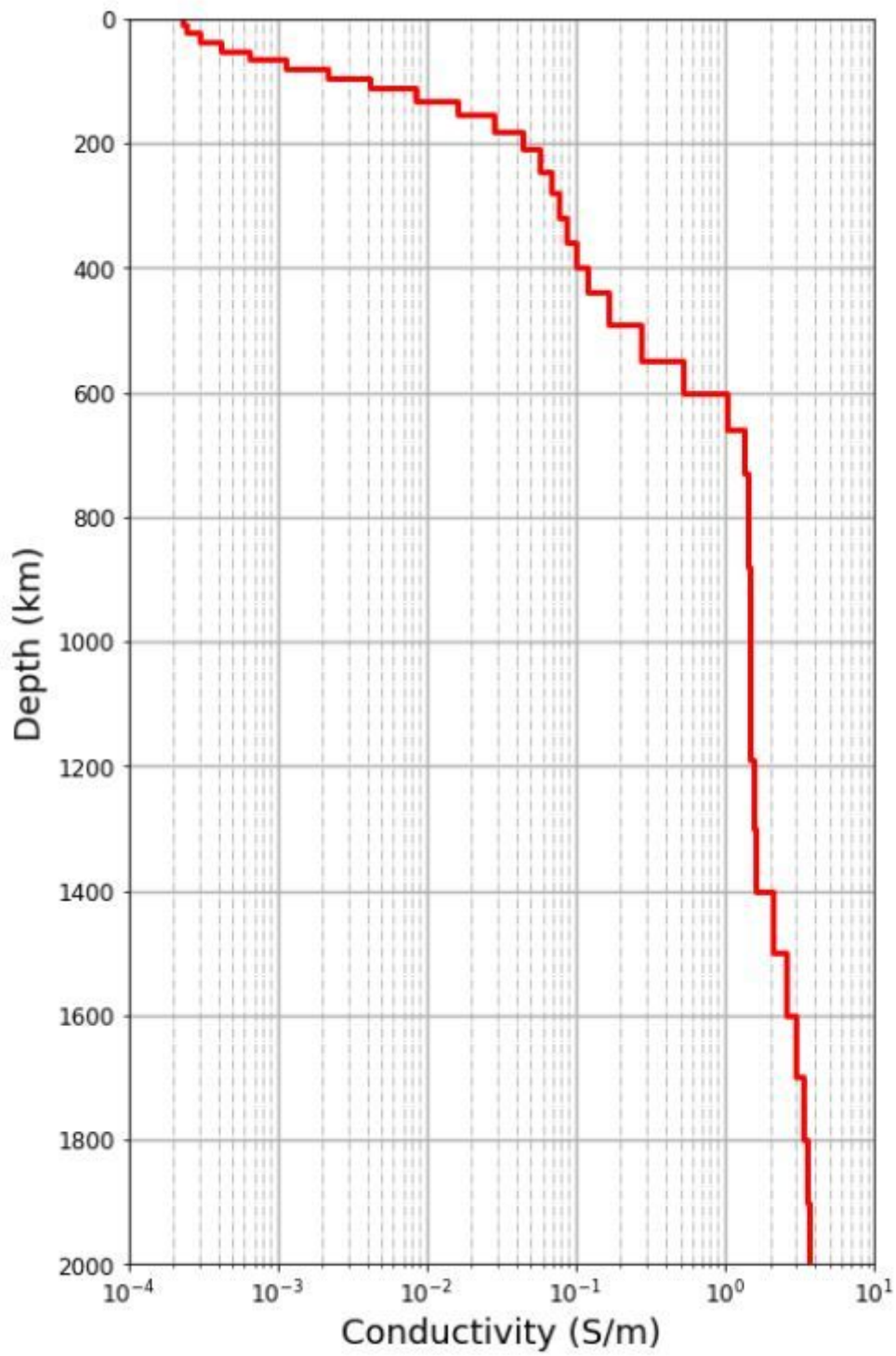


Figure 3

1-D global conductivity profile (from Grayver et al, 2017) used in this study for the crust and mantle beneath the 3-D (oceanic) modeling domains.

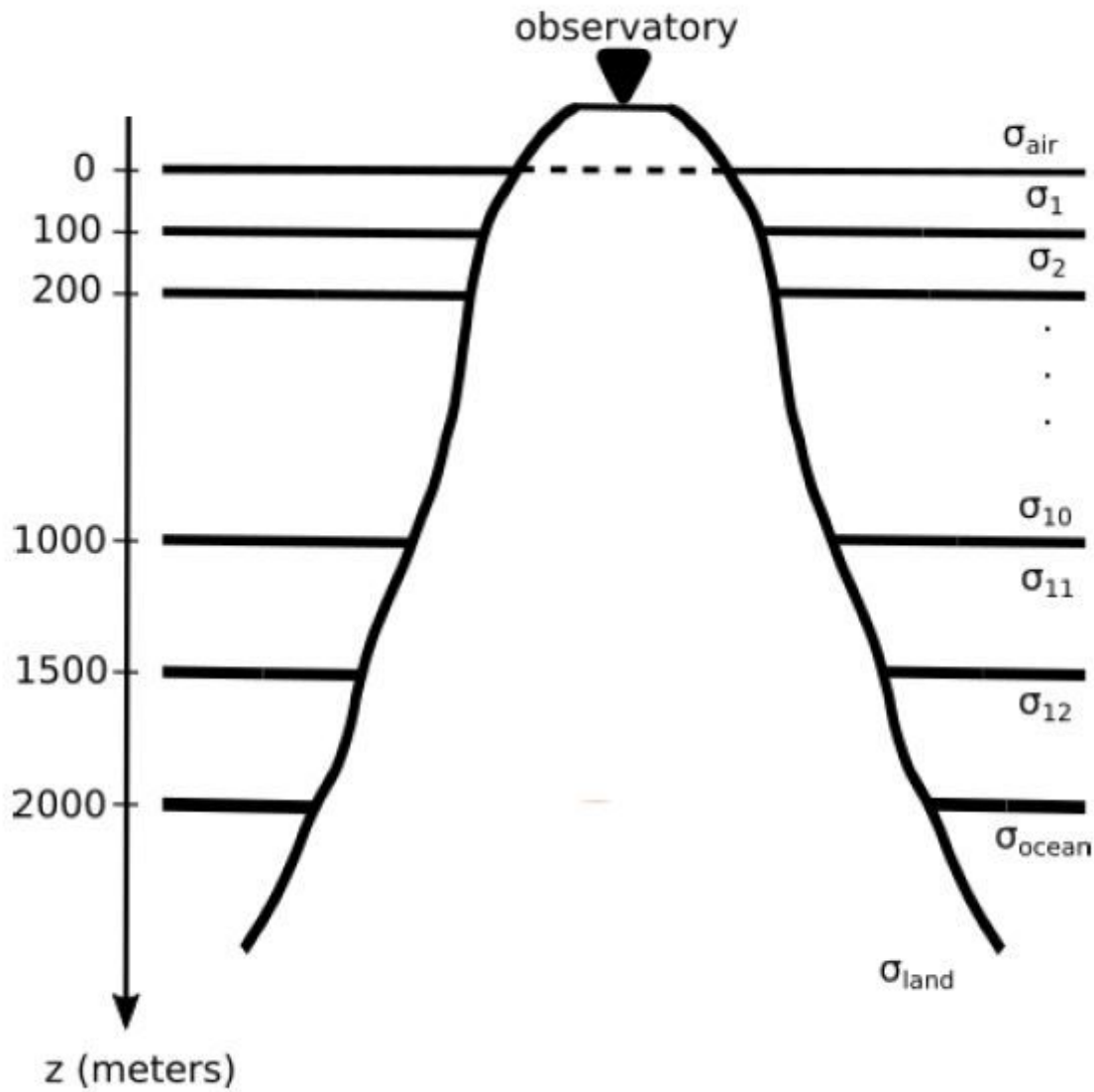


Figure 4

Vertical parametrization of the oceanic conductivity distribution in the 3-D modeling domain. σ_1 to σ_{12} is the respective water layer's conductivity, set to the layer's average conductivity calculated from the global ocean conductivity model. σ_{ocean} is the deep (below 2000 m) ocean conductivity, which is set to 3.2 S/m. σ_{land} and σ_{air} are the landmass and air conductivity set to 0.01 S/m and 10×10^8 S/m, respectively.

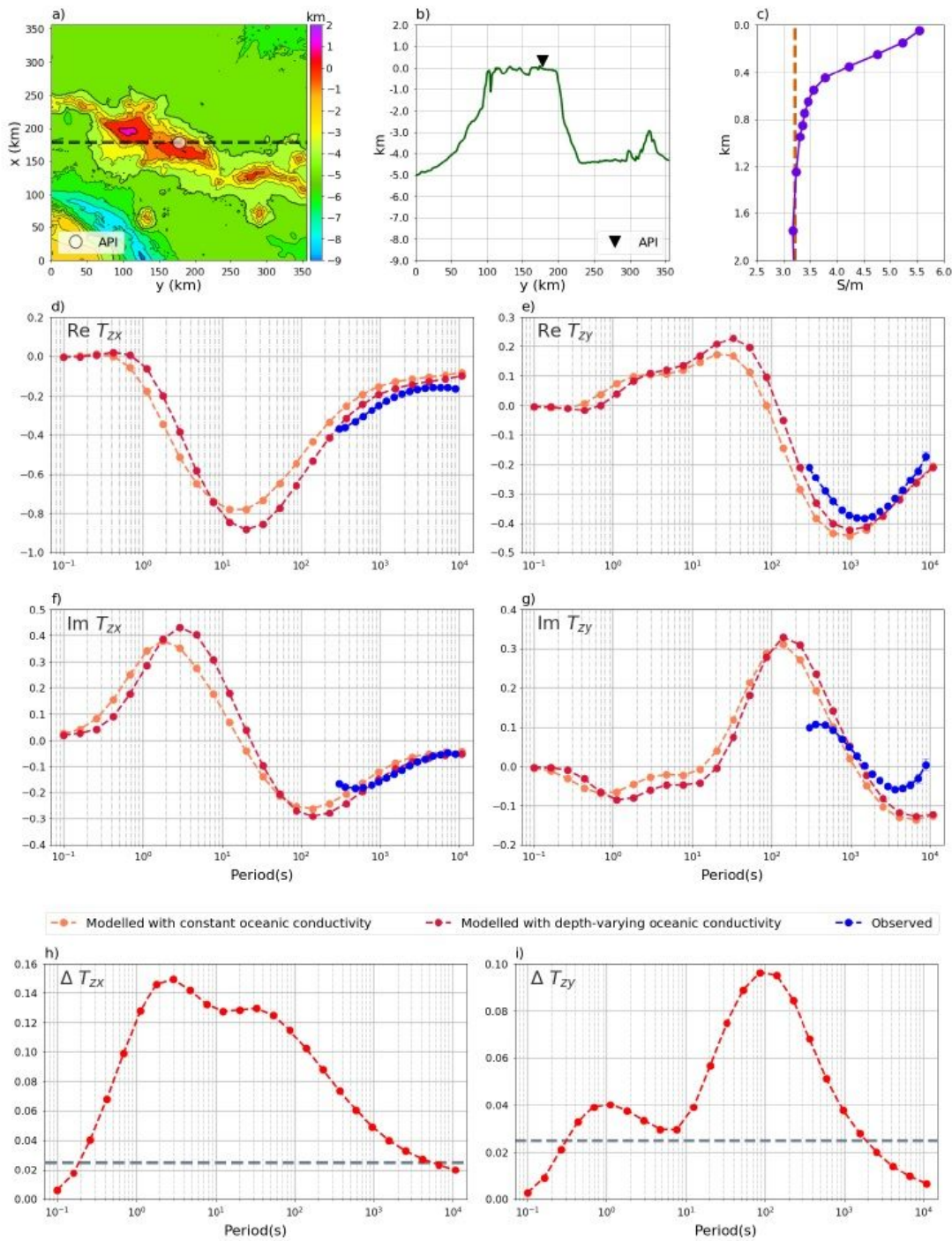


Figure 5

Results for Apia observatory (API). (a) Map of bathymetry/topography; dashed line indicates location of prole shown in panel (b). (b) West-East oriented bathymetry prole. (c) Regional depth-varying (purple) oceanic conductivity and constant reference oceanic conductivity (3.2 S/m, orange dashed line). (d) to (g) Real and imaginary parts for x and y components of tippers computed in the model with depth-varying (orange dots and dashed line) and depth-constant (red dots and dashed line) oceanic

conductivity. (h) Difference for the computed tipper x component between depth-varying and depth-constant ocean conductivity, see text for details. Dashed grey line indicates the threshold of 0.025. (i) Same as (h), but for the y component.

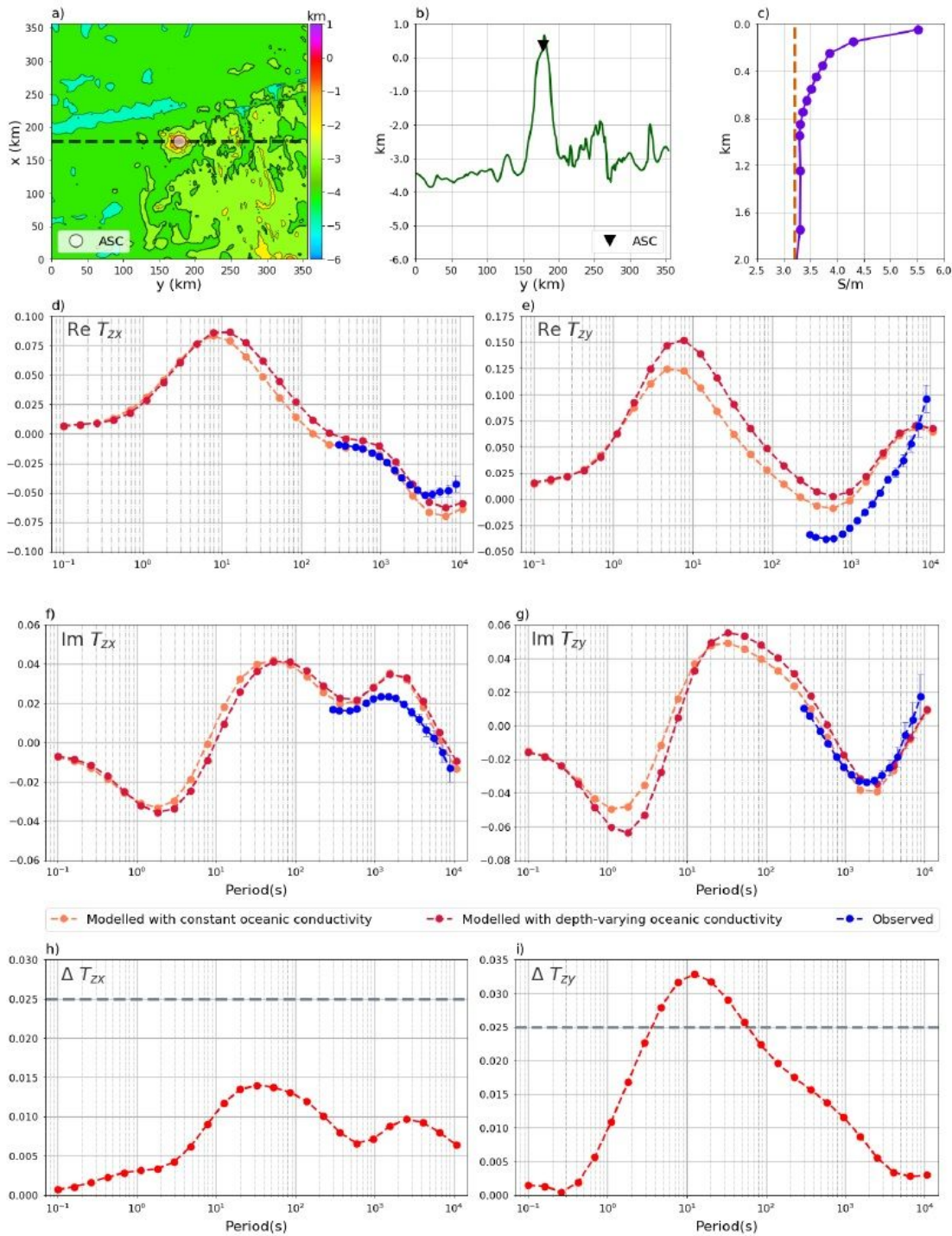


Figure 6

Same as Figure 5, but for Ascension Island observatory (ASC).

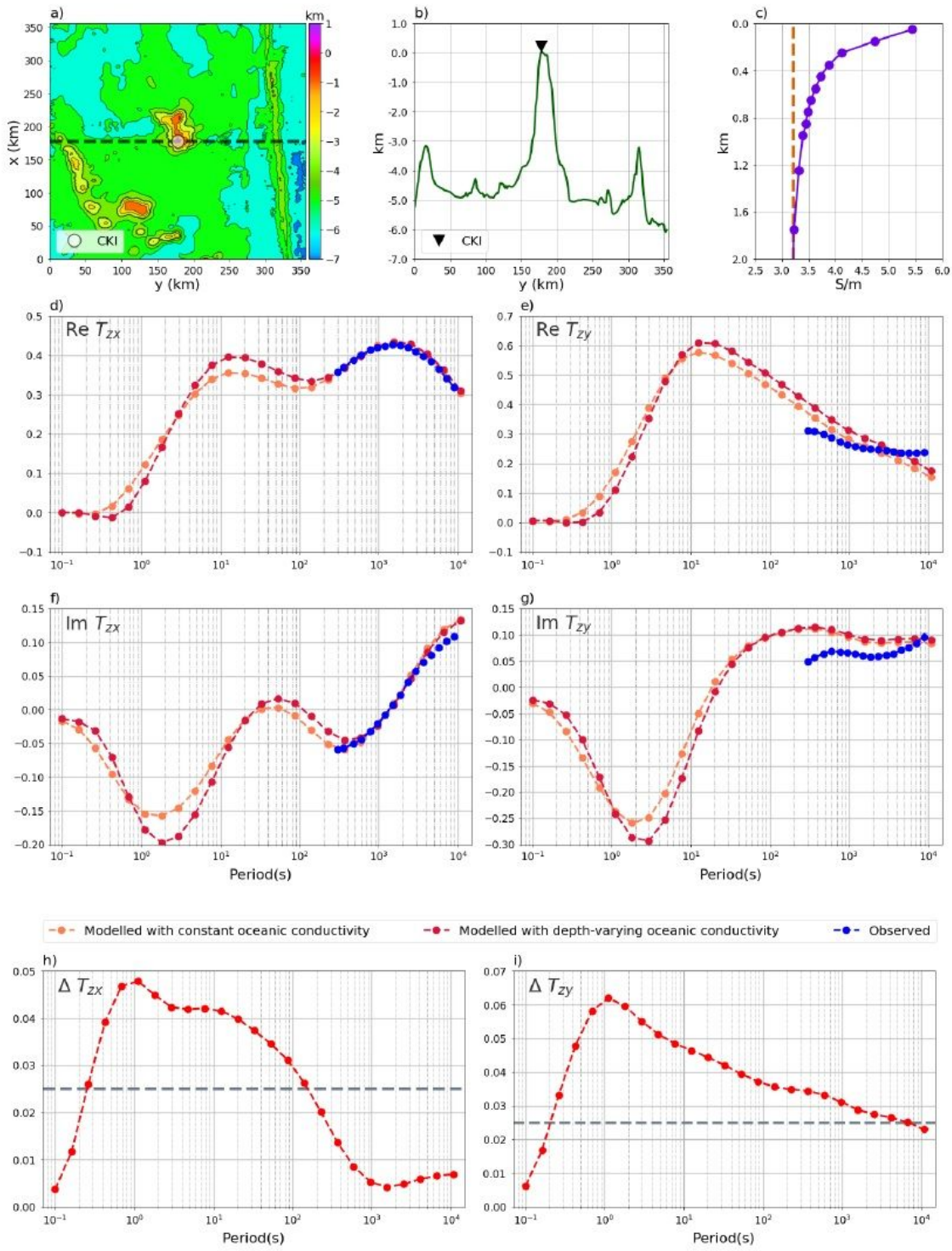


Figure 7

Same as Figure 5, but for Cocos-Keeling Islands observatory (CKI).

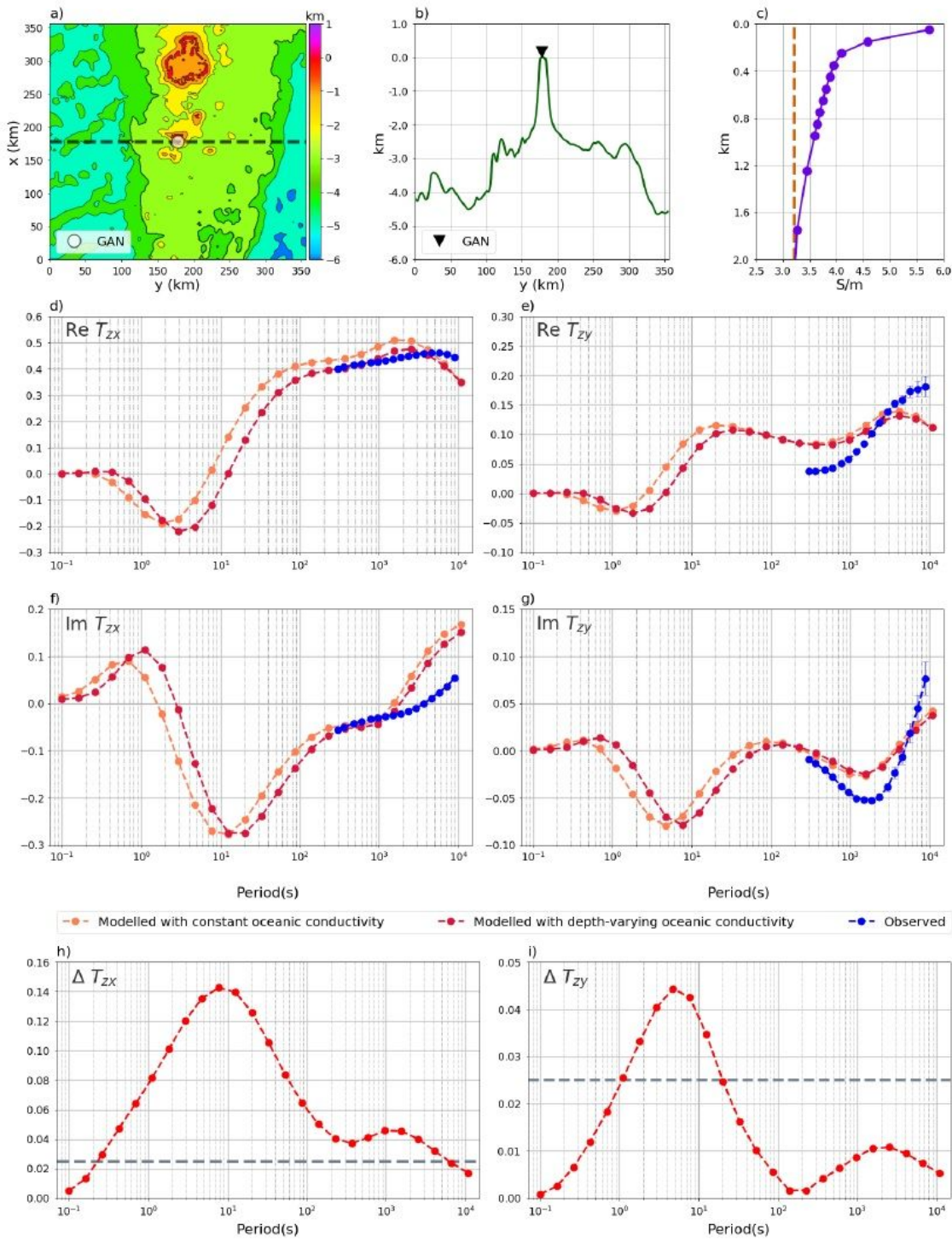


Figure 8

Same as Figure 5, but for Gan observatory (GAN).

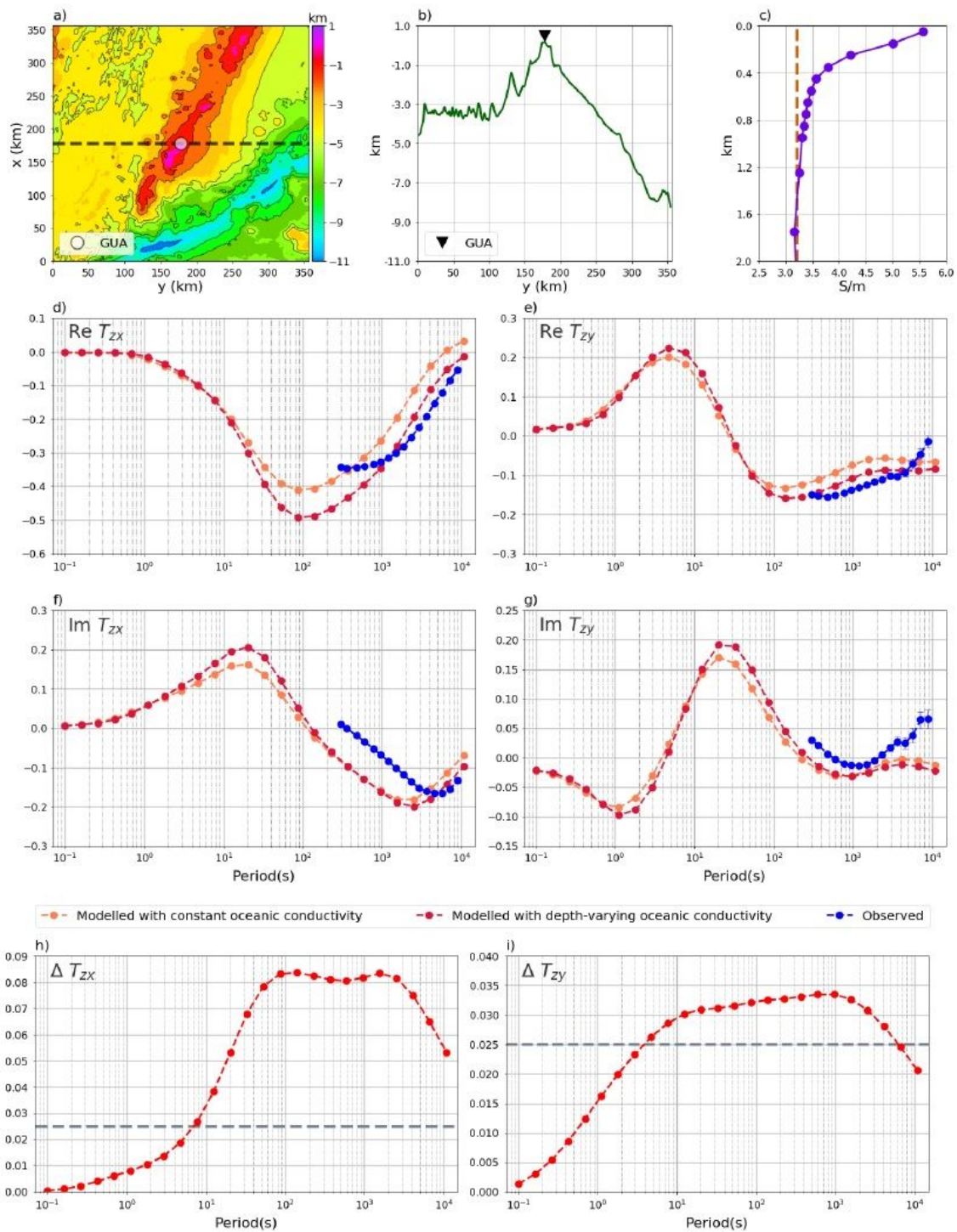


Figure 9

Same as Figure 5, but for Guam observatory (GUA).

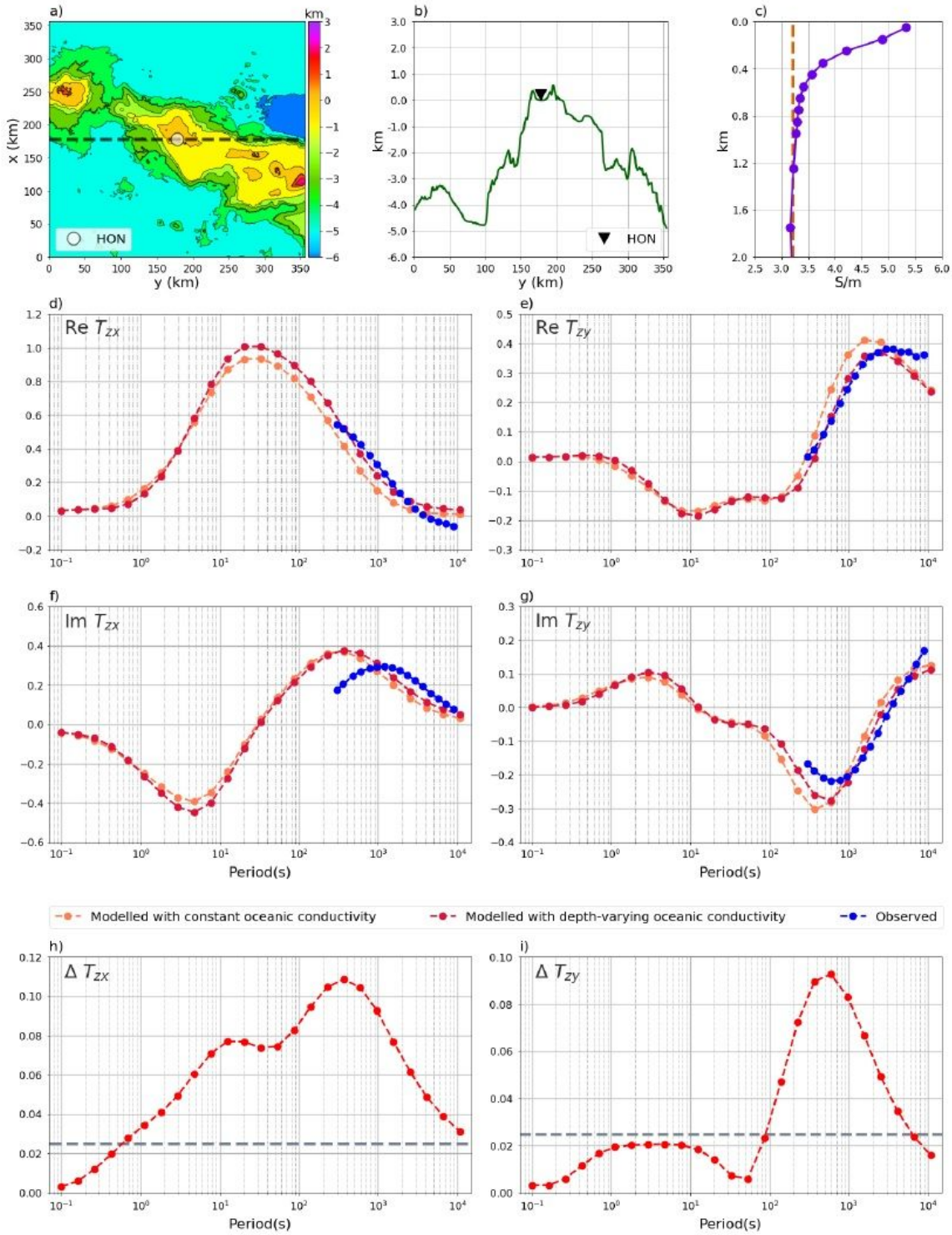


Figure 10

Same as Figure 5, but for Honolulu observatory (HON).

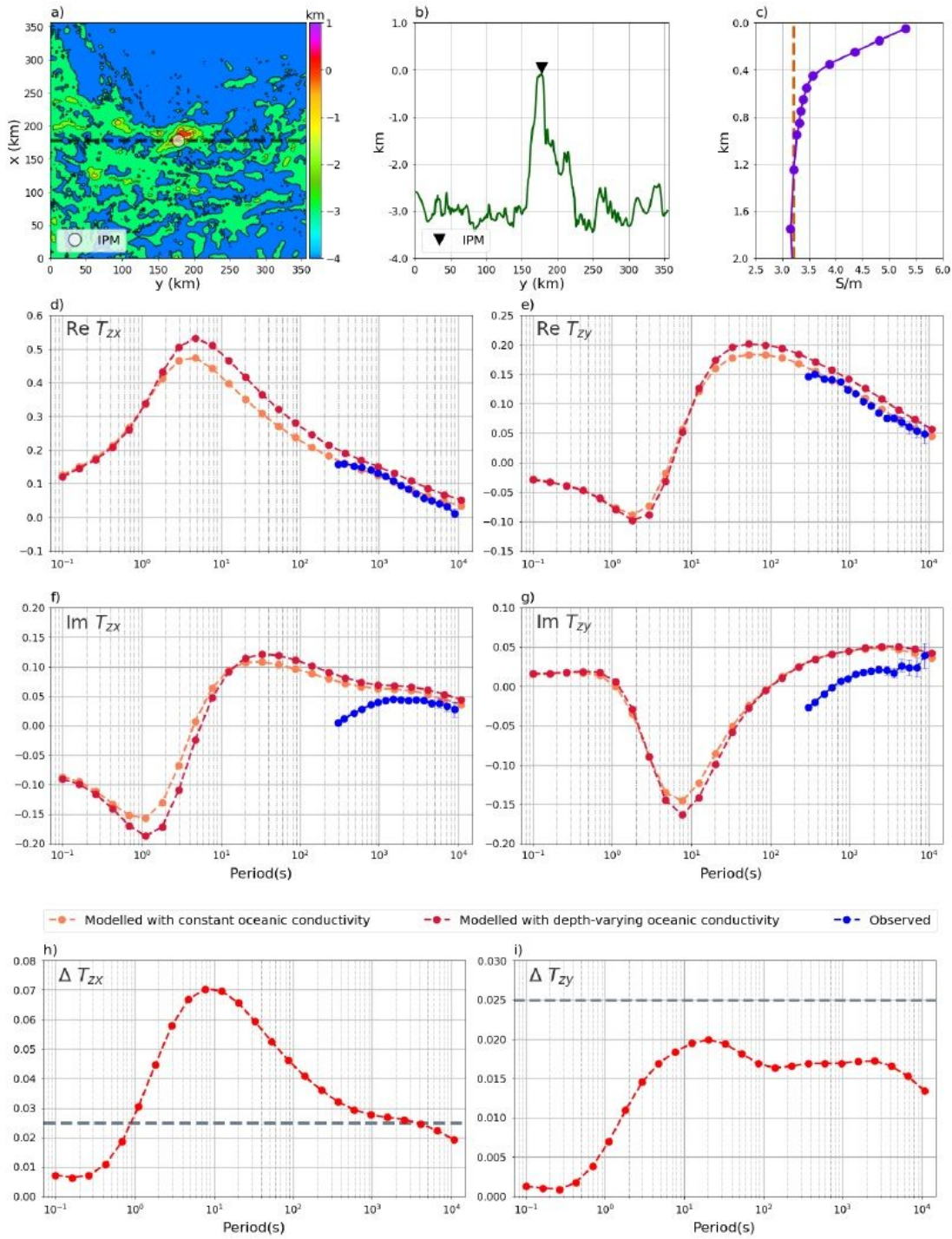


Figure 11

Same as Figure 5, but for Easter Island observatory (IPM).

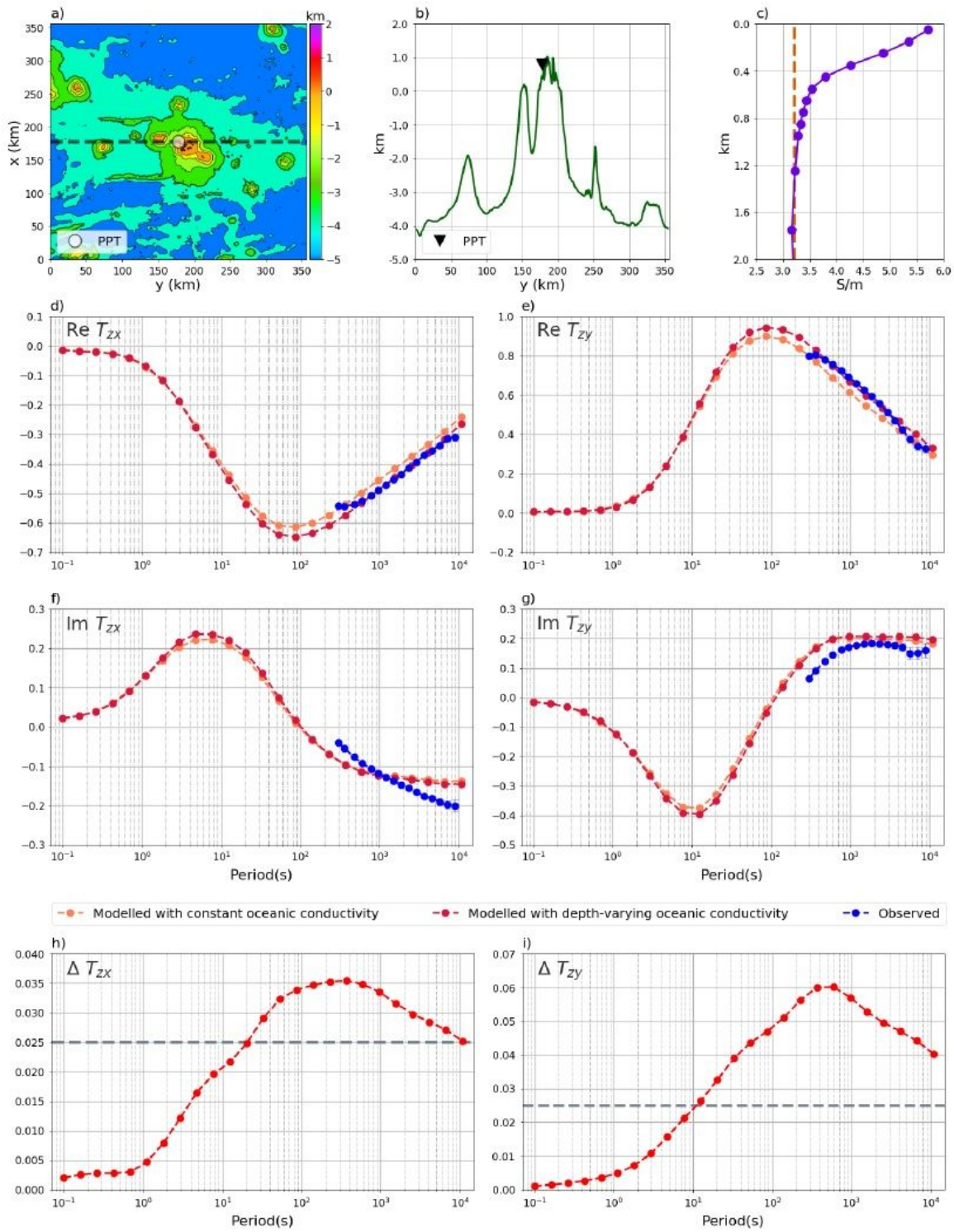


Figure 12

Same as Figure 5, but for Pamatai observatory (PPT).

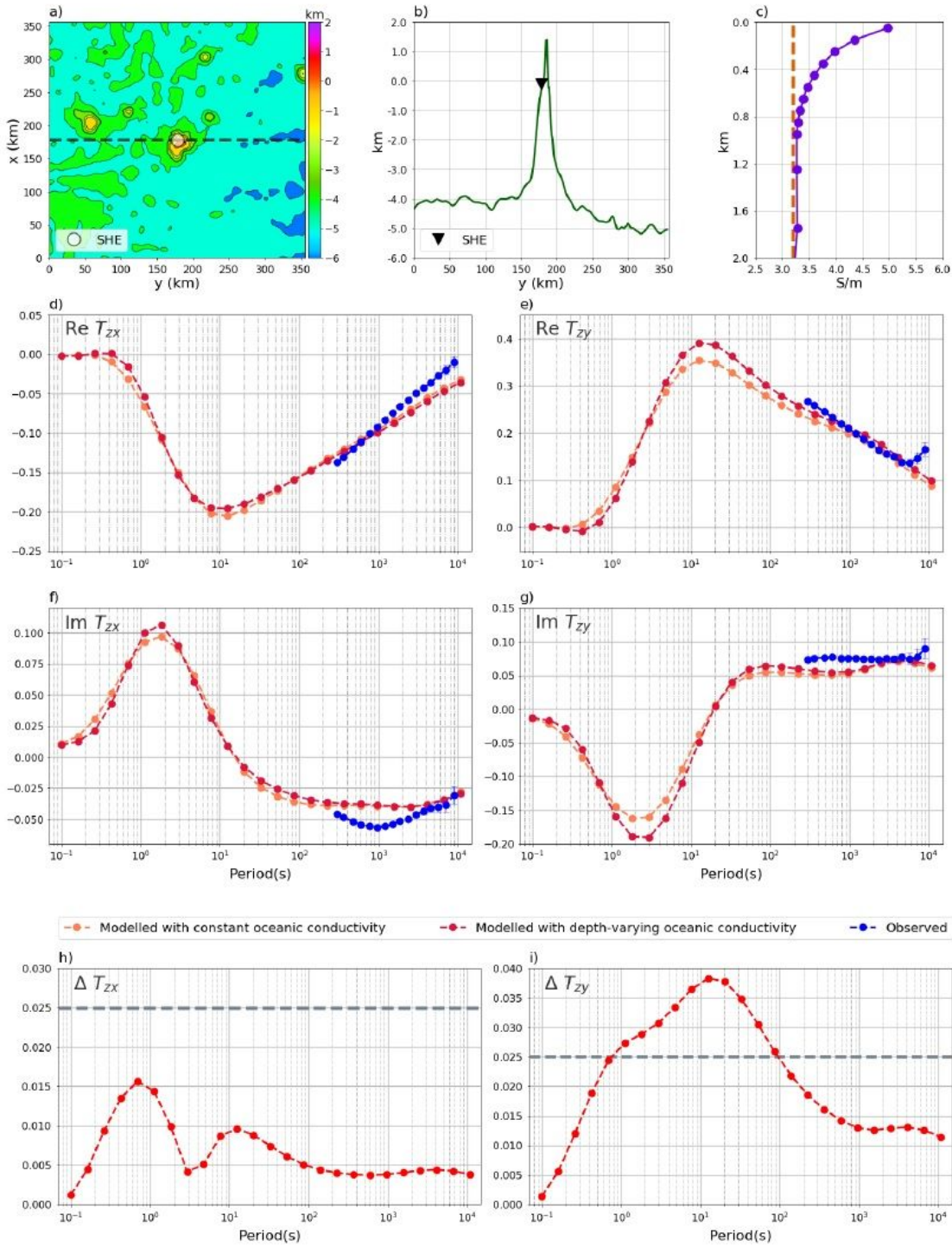


Figure 13

Same as Figure 5, but for St. Helena observatory (SHE).

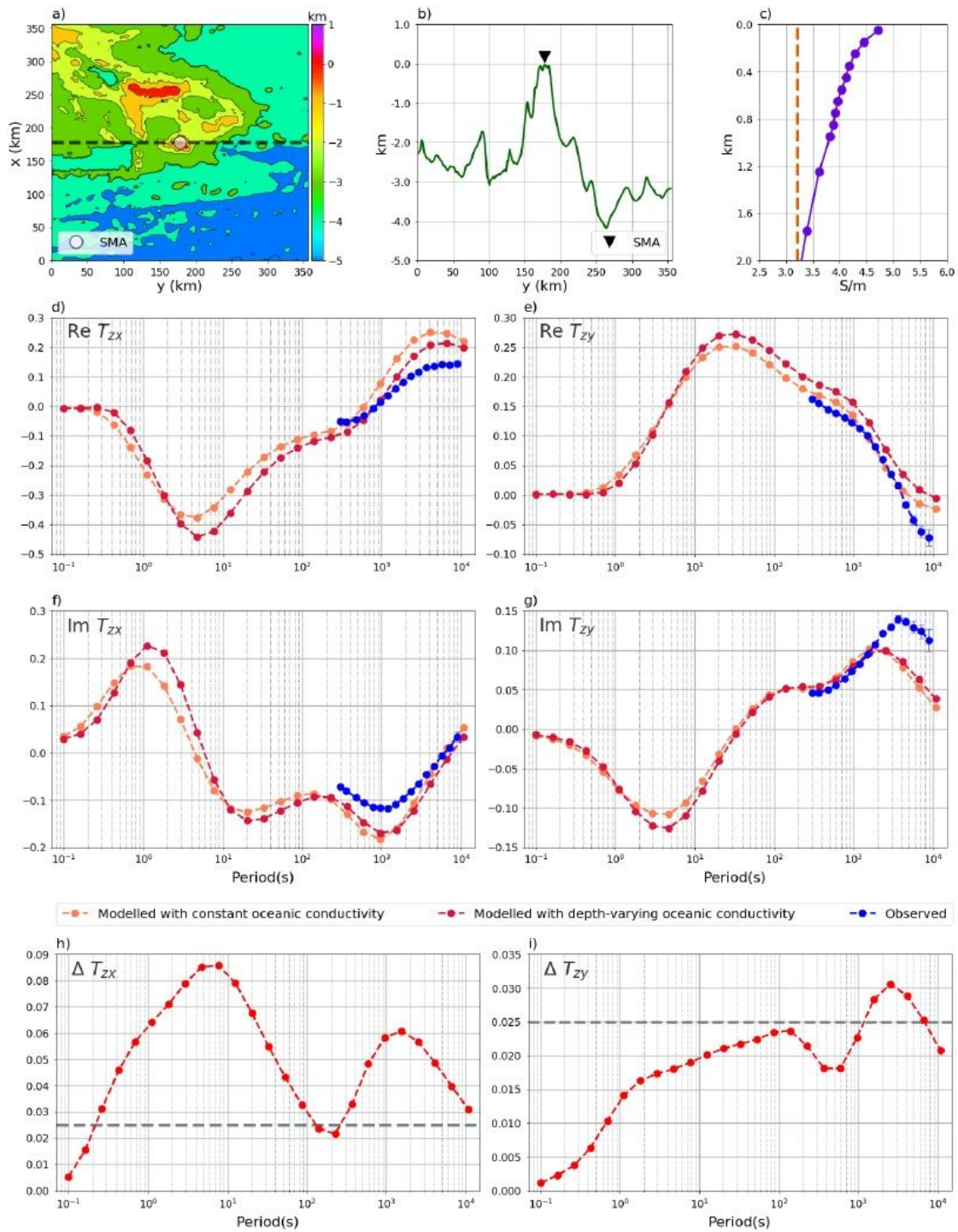


Figure 14

Same as Figure 5, but for Santa-Maria/Azores observatory (SMA).

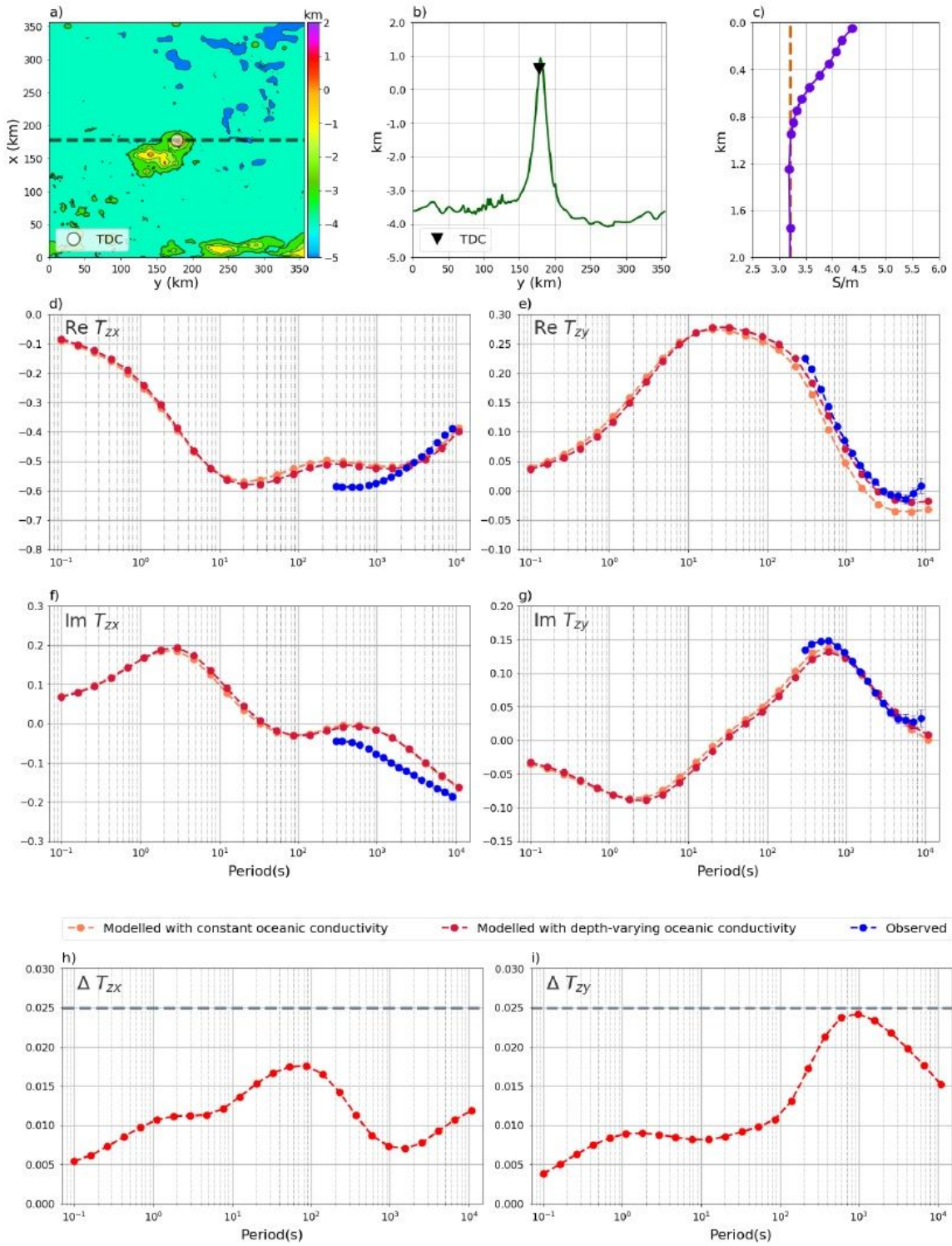


Figure 15

Same as Figure 5, but for Tristan da Cunha observatory (TDC).

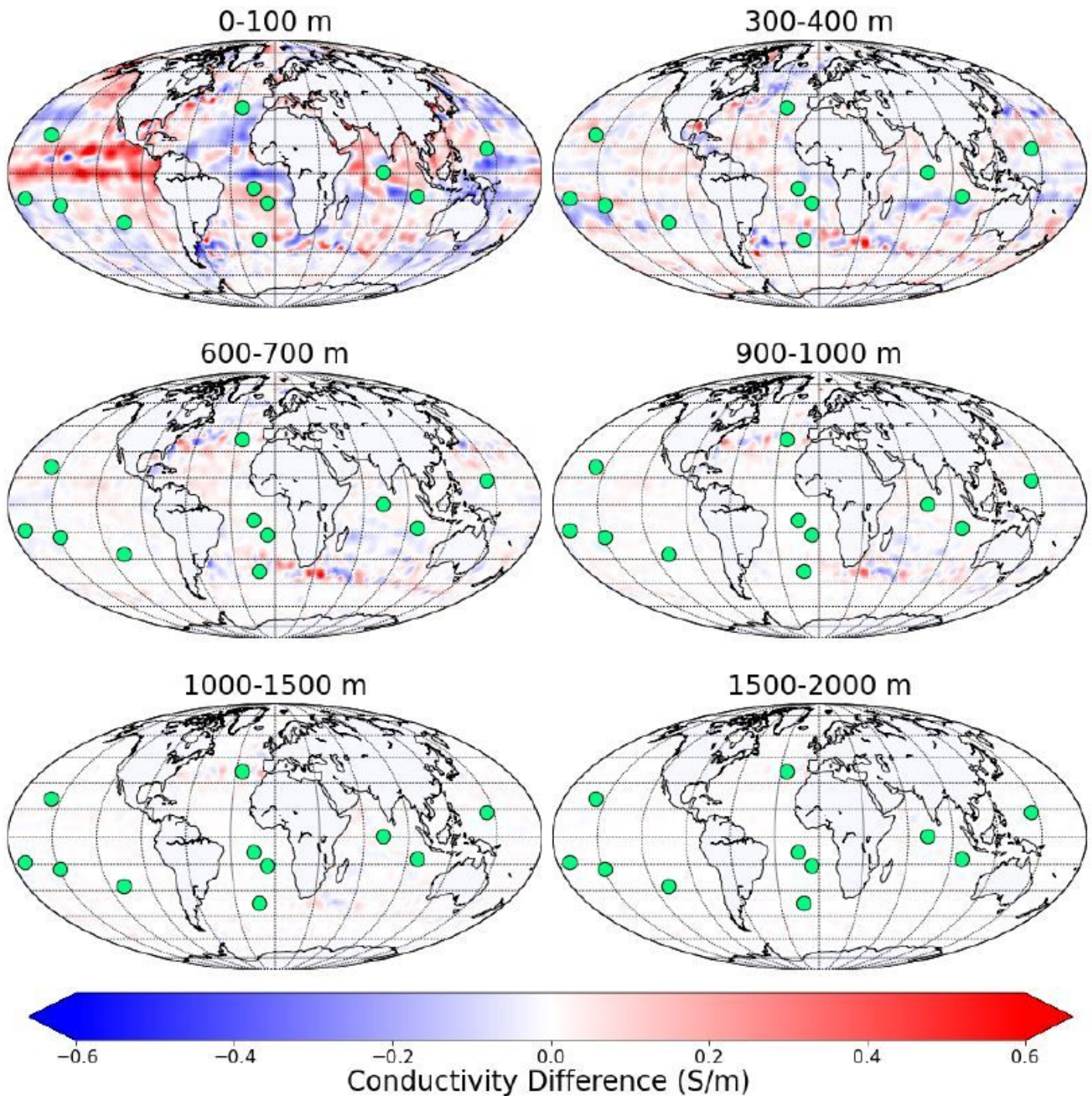


Figure 16

Global maps of difference between 2015 December and June oceanic conductivity models at six depth intervals. Green circles denote locations of geomagnetic observatories used in this study. Note: The designations employed and the presentation of the material on this map do not imply the expression of any opinion whatsoever on the part of Research Square concerning the legal status of any country, territory, city or area or of its authorities, or concerning the delimitation of its frontiers or boundaries. This map has been provided by the authors.

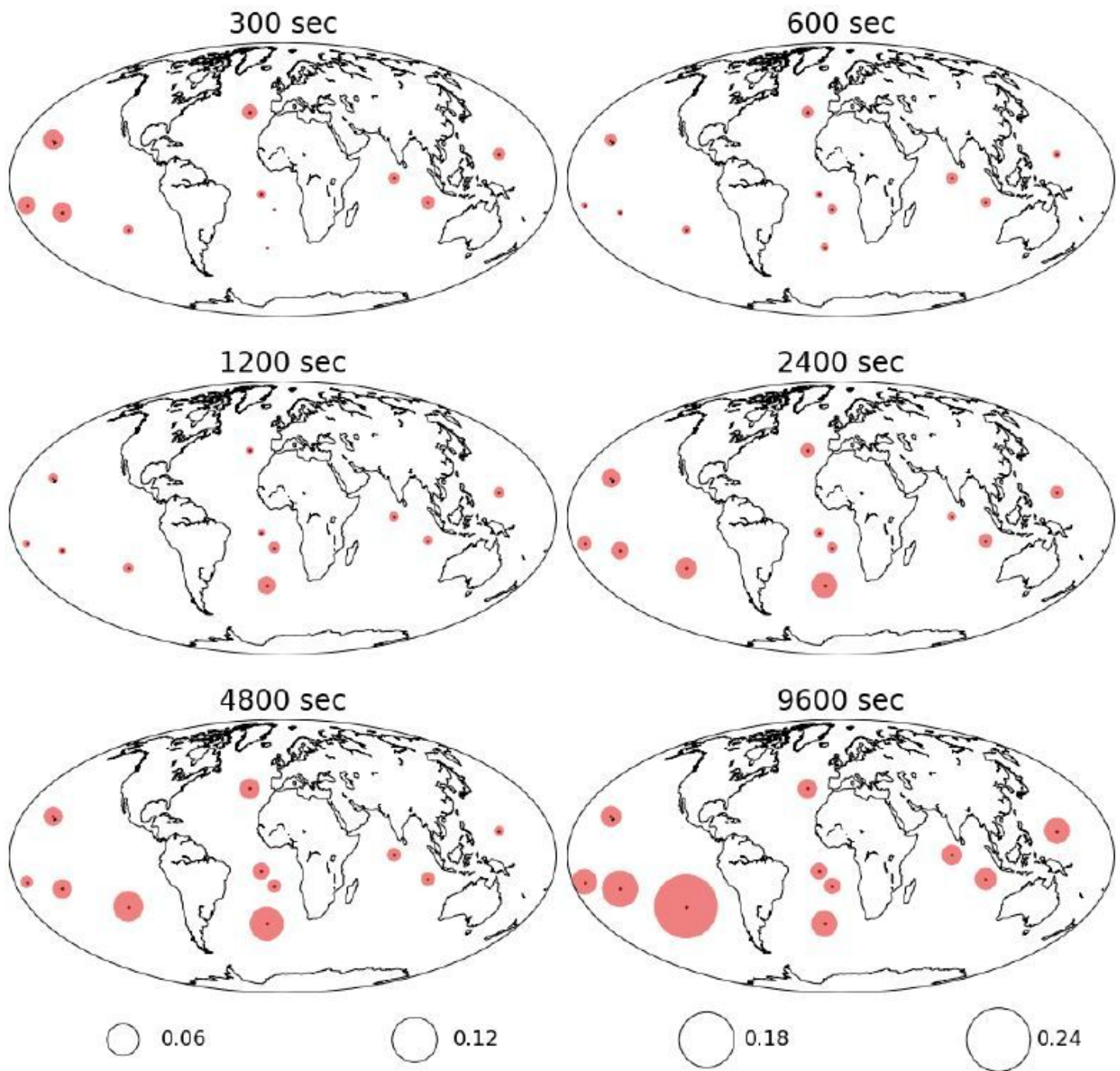


Figure 17

Difference between "December" and "June" Tzx at island observatories, shown as filled circles. "Experimental" and "modeled" differences are colored by light and dark red, respectively. The size of circles below the plots indicates four ranges of differences. Note: The designations employed and the presentation of the material on this map do not imply the expression of any opinion whatsoever on the part of Research Square concerning the legal status of any country, territory, city or area or of its

authorities, or concerning the delimitation of its frontiers or boundaries. This map has been provided by the authors.

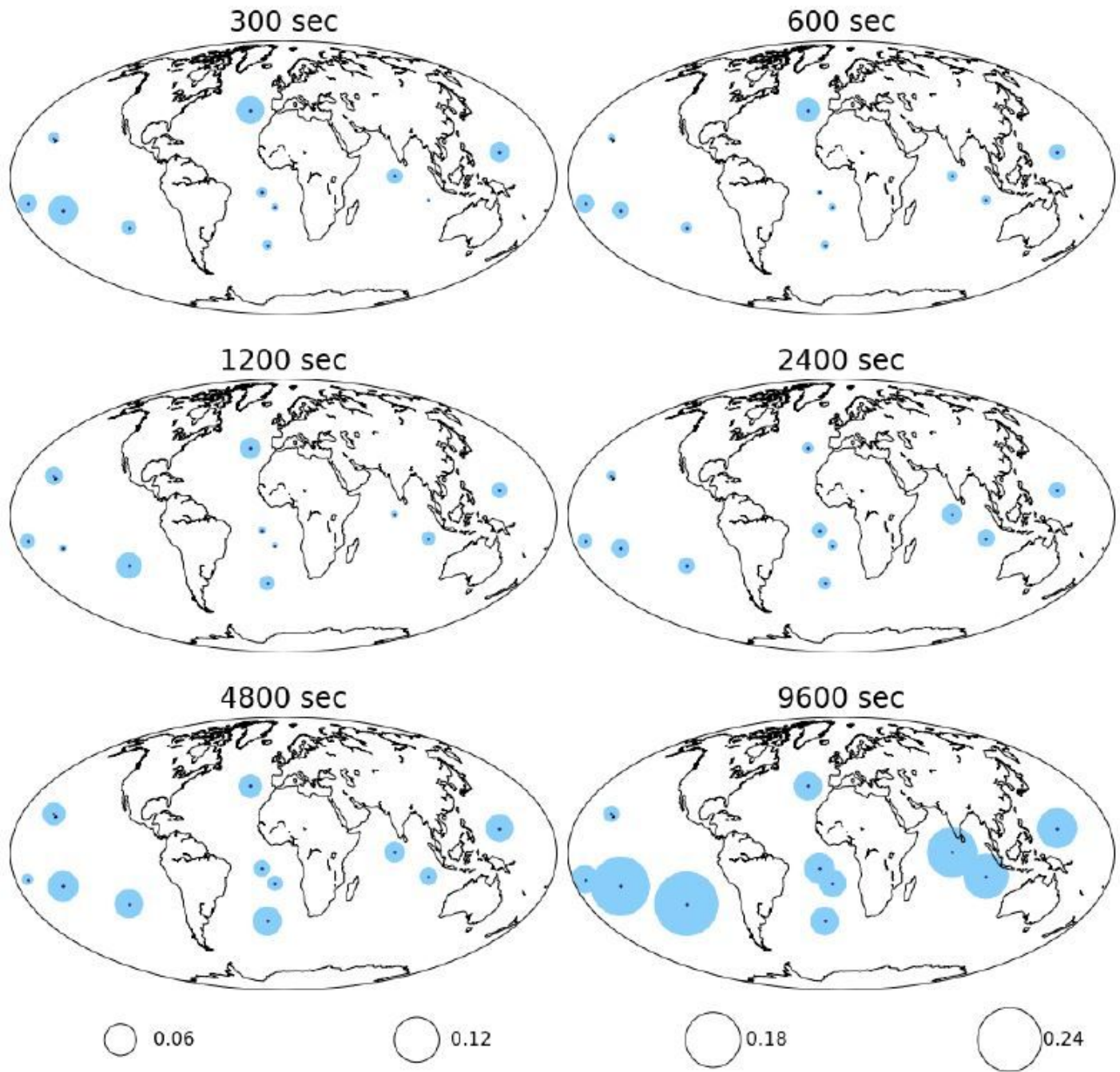


Figure 18

Difference between "December" and "June" Tzy at island observatories, shown as filled circles. "Experimental" and "modeled" differences are colored by light and dark blue, respectively. The size of circles below the plots indicates four ranges of differences. Note: The designations employed and the presentation of the material on this map do not imply the expression of any opinion whatsoever on the part of Research Square concerning the legal status of any country, territory, city or area or of its

authorities, or concerning the delimitation of its frontiers or boundaries. This map has been provided by the authors.

Supplementary Files

This is a list of supplementary files associated with this preprint. Click to download.

- [GraphicalAbstract.png](#)